



Multiwavelength Observations of a Jet Launch in Real Time from the Post-changing-look Active Galaxy 1ES 1927+654

Sibasish Laha^{1,2,3,34} , Eileen T. Meyer⁴ , Dev R. Sadaula^{1,2,3} , Ritesh Ghosh^{1,2,3,5} , Dhrubojyoti Sengupta² , Megan Masterson⁶ , Onic I. Shuvo⁴ , Matteo Guainazzi⁷ , Claudio Ricci^{8,9} , Mitchell C. Begelman¹⁰ , Alexander Philippov¹¹ , Rostom Mbarek^{12,13,33} , Amelia M. Hankla^{12,13,33} , Erin Kara⁶ , Francesca Panessa¹⁴ , Ehud Behar¹⁵ , Haocheng Zhang^{1,2,3} , Fabio Pacucci^{16,17} , Main Pal¹⁸ , Federica Ricci^{19,20} , Ilaria Villani^{19,20} , Susanna Bisogni²¹ , Fabio La Franca¹⁹ , Stefano Bianchi¹⁹ , Gabriele Bruni¹⁴ , Samantha Oates²² , Cameron Hahn⁴ , Matt Nicholl²³ , S. Bradley Cenko^{1,12} , Sabyasachi Chattopadhyay^{24,25} , Josefa Becerra González^{26,27} , J. A. Acosta-Pulido^{26,27} , Suvendu Rakshit²⁸ , Jiří Svoboda²⁹ , Luigi Gallo³⁰ , Adam Ingram³¹ , and Darshan Kakkad³² 

¹ Astrophysics Science Division, NASA Goddard Space Flight Center, Greenbelt, MD 20771, USA; sib.laha@gmail.com, sibasish.laha@nasa.gov

² Center for Space Science and Technology, University of Maryland Baltimore County, 1000 Hilltop Circle, Baltimore, MD 21250, USA

³ Center for Research and Exploration in Space Science and Technology, NASA/GSFC, Greenbelt, MD 20771, USA

⁴ Department of Physics, University of Maryland Baltimore County, 1000 Hilltop Circle, Baltimore, MD 21250, USA

⁵ MKHS, Murshidabad, West Bengal, India 742401, India

⁶ MIT Kavli Institute for Astrophysics and Space Research, Massachusetts Institute of Technology, Cambridge, MA 02139, USA

⁷ European Space Agency (ESA), European Space Research and Technology Centre (ESTEC), Keplerlaan 1, 2201 AZ Noordwijk, The Netherlands

⁸ Instituto de Estudios Astrofísicos, Facultad de Ingeniería y Ciencias, Universidad Diego Portales, Av. Ejército Libertador 441, Santiago, Chile

⁹ Kavli Institute for Astronomy and Astrophysics, Peking University, Beijing 100871, People's Republic of China

¹⁰ JILA, University of Colorado and National Institute of Standards and Technology, 440 UCB, Boulder, CO 80309-0440, USA

¹¹ Department of Physics, University of Maryland, College Park, MD 20742, USA

¹² Joint Space-Science Institute, University of Maryland, College Park, MD 20742, USA

¹³ Department of Astronomy, University of Maryland, College Park, MD 20742, USA

¹⁴ INAF—Istituto di Astrofisica e Planetologia Spaziali, Via del Fosso del Cavaliere 100, Roma, 00133, Italy

¹⁵ Department of Physics, Technion, Haifa 32000, Israel

¹⁶ Center for Astrophysics | Harvard & Smithsonian, Cambridge, MA 02138, USA

¹⁷ Black Hole Initiative, Harvard University, Cambridge, MA 02138, USA

¹⁸ Department of Physics, Sri Venkateswara College, University of Delhi, Benito Juarez Road, Dhaura Kuan, New Delhi 110021, India

¹⁹ Dipartimento di Matematica e Fisica, Università degli Studi Roma Tre, Via della Vasca Navale 84, 00146, Roma, Italy

²⁰ INAF-Osservatorio Astronomico di Roma, via Frascati 33, 00040 Monteporzio Catone, Italy

²¹ INAF—Istituto di Astrofisica Spaziale e Fisica Cosmica Milano, Via Corti 12, 20133 Milano, Italy

²² Department of Physics, Lancaster University, Lancaster LA1 4YB, UK

²³ Astrophysics Research Centre, School of Mathematics and Physics, Queens University Belfast, Belfast BT7 1NN, UK

²⁴ South African Astronomical Observatory, 1 Observatory Rd., Observatory, Cape Town, 7925, South Africa

²⁵ Centre for Space Research, North-West University, Potchefstroom 2520, South Africa

²⁶ Instituto de Astrofísica de Canarias (IAC), E-38200 La Laguna, Tenerife, Spain

²⁷ Universidad de La Laguna (ULL), Departamento de Astrofísica, E-38206 La Laguna, Tenerife, Spain

²⁸ Aryabhata Research Institute of Observational Sciences (ARIES), Manora Peak, Nainital, 263002, India

²⁹ Astronomical Institute of the Czech Academy of Sciences, Boční II 1401/1, 14100 Praha 4, Czech Republic

³⁰ Department of Astronomy and Physics, Saint Mary's University, 923 Robie Street, Halifax, NS B3H 3C3, Canada

³¹ School of Mathematics Statistics and Physics, Newcastle University, NE1 7RU, UK

³² Centre for Astrophysics Research, University of Hertfordshire, Hatfield, AL10 9AB, UK

Received 2024 September 6; revised 2025 January 1; accepted 2025 January 22; published 2025 March 4

Abstract

We present results from a high-cadence multiwavelength observational campaign of the enigmatic changing-look active galactic nucleus 1ES 1927+654 from 2022 May to 2024 April, coincident with an unprecedented radio flare (an increase in flux by a factor of ~ 60 over a few months) and the emergence of a spatially resolved jet at 0.1–0.3 pc scales. Companion work has also detected a recurrent quasi-periodic oscillation (QPO) in the 2–10 keV band with an increasing frequency (1–2 mHz) over the same period. During this time, the soft X-rays (0.3–2 keV) monotonically increased by a factor of ~ 8 , while the UV emission remained nearly steady with $< 30\%$ variation and the 2–10 keV flux showed variation by a factor $\lesssim 2$. The weak variation of the 2–10 keV X-ray emission and the stability of the UV emission suggest that the magnetic energy density and accretion rate are relatively unchanged and that the jet could be launched owing to a reconfiguration of the magnetic field (toroidal to poloidal) close to the black hole. Advecting poloidal flux onto the event horizon would trigger the Blandford–Znajek mechanism, leading to the onset of the jet. The concurrent softening of the coronal slope (from $\Gamma = 2.70 \pm 0.04$ to $\Gamma = 3.27 \pm 0.04$), the appearance of a QPO, and the low coronal temperature ($kT_e = 8_{-3}^{+8}$ keV) during the radio

³³ Neil Gehrels Fellow.

³⁴ Corresponding author.



Original content from this work may be used under the terms of the [Creative Commons Attribution 4.0 licence](https://creativecommons.org/licenses/by/4.0/). Any further distribution of this work must maintain attribution to the author(s) and the title of the work, journal citation and DOI.

outburst suggest that the poloidal field reconfiguration can significantly impact coronal properties and thus influence jet dynamics. These extraordinary findings in real time are crucial for coronal and jet plasma studies, particularly as our results are independent of coronal geometry.

Unified Astronomy Thesaurus concepts: [Active galaxies \(17\)](#); [Supermassive black holes \(1663\)](#)

1. Introduction

Active galactic nuclei (AGN) are a diverse class of sources that can be detected at nearly every wave band from radio to gamma rays and over a very wide range of luminosity, with bolometric power up to 10^{48} erg s⁻¹ (F. Duras et al. 2020; I. Saccheo et al. 2023). Powered by accretion onto the central supermassive black hole (SMBH), AGN activity has been shown to impact not only the evolution of the host galaxy but also the surrounding environment (J. Kormendy & L. C. Ho 2013). In part due to its very small size, the exact physics and geometry of the central engine in AGN are still not clearly understood. For example, we still do not have a clear understanding of the angular momentum transfer mechanisms that help the accretion flow in the disk. The nature of the accretion flow (i.e., accretion mode) varies widely over the ~ 6 – 7 orders of magnitude in observed mass accretion rate. Both the accretion mode and accretion rate play an important role in the production of jets and outflows, which go on to influence not just the immediate vicinity of the central engine and the host galaxy but also the larger-scale environments (A. C. Fabian 2012; M. C. Begelman et al. 2022).

Although spectral and flux variability is quite common in AGN across a range of wavelengths (M. Elvis et al. 1994; T. Hovatta et al. 2007; C. Ricci et al. 2017; S. Laha et al. 2024), in some rare cases we find rapid changes in the optical spectral type (type 2 to type 1) and/or order-of-magnitude flares in multiwavelength bands in a time span of months to years, possibly caused/triggered by rapid accretion mode and/or accretion rate changes. This class of AGN is popularly known as “changing-look” AGN (CL-AGN; S. M. LaMassa et al. 2015; B. Trakhtenbrot et al. 2019; C. Ricci & B. Trakhtenbrot 2023), and they serve as ideal sources to probe the physics of the central engine in real time and its connection with the immediate surroundings (C. Ricci & B. Trakhtenbrot 2023).

1ES 1927+654 is an enigmatic CL-AGN with an SMBH mass of $1.36 \times 10^6 M_{\odot}$ (R. Li et al. 2022) at a redshift of $z=0.017$. The source first exhibited a dramatic optical/UV outburst starting in 2017 December (B. Trakhtenbrot et al. 2019; C. Ricci et al. 2020) and has since showed unprecedented behavior, particularly in the X-rays, when compared to other known CL-AGN (C. Ricci et al. 2020, 2021; S. Laha et al. 2022; M. Masterson et al. 2022). Earlier optical and X-ray studies (T. Boller et al. 2003; L. C. Gallo et al. 2013) have shown that the source was a true type 2 AGN pre-outburst (F. Panessa & L. Bassani 2002; S. Bianchi et al. 2012); despite having only narrow emission lines in the optical spectrum, there was no evidence of line-of-sight obscuration at any wavelength. After the optical/UV flare in 2018, broad emission lines appeared with a lag of ~ 100 days and remained visible for several months after. Conversely, the 2–10 keV coronal hard X-ray emission completely vanished by 2018 August (C. Ricci et al. 2020, 2021; S. Laha et al. 2022; C. Ricci & B. Trakhtenbrot 2023), only to return a few months later, eventually flaring up to ~ 10 times the preflare value. There has been essentially no correlation between the X-rays and the optical/UV both during the 2018 flare and in the several years since.

Figure 1 illustrates the timeline of the most important events and phases of the source since 2011 May.

After the flare, the UV flux monotonically dimmed with a slope $t^{-0.91 \pm 0.04}$ (S. Laha et al. 2022), returning to a near preflare value after ~ 1200 days of the initial flare. The parsec-scale radio flux density at 5 GHz, as measured by the Very Long Baseline Array (VLBA), showed a minimum (a factor of 4 below the preflare value) at the time when the X-ray flux was low, and it gradually increased over the next 2 yr.

Some have argued that the 2018 flare was a tidal disruption event (TDE) in an existing AGN (B. Trakhtenbrot et al. 2019; C. Ricci et al. 2020, 2021; M. Masterson et al. 2022), while others propose a magnetic flux inversion scenario (N. Scepi et al. 2021; S. Laha et al. 2022). Our recent study (R. Ghosh et al. 2023) covering the post-CL phase detected an emerging bright soft state with the soft X-ray flux reaching ~ 5 times that of the preflare value, while the hard X-rays and UV showed no significant new variation. 1ES 1927+654 has an Eddington ratio³⁵ (as measured on 2023 May using broadband spectral modeling of the UV–X-ray spectral energy distribution (SED)) of $\lambda_{\text{Edd}} = 0.23$ (R. Ghosh et al. 2023). This value of the Eddington ratio would likely place 1ES 1927+654 in the radiatively efficient, thin accretion disk regime (see, e.g., I. D. Novikov & K. S. Thorne 1973; N. I. Shakura & R. A. Sunyaev 1973), with typical radiative efficiencies of $\sim 10\%$. However, during the CL event (2018–2021) the source was mostly accreting at the Eddington rate (R. Li et al. 2024).

Our companion paper (Masterson et al. 2025, Nature, in press) finds significant short-term variability in the X-ray light curve and has detected a consistent quasi-periodic oscillation (QPO) predominantly in the 2–10 keV band. The QPO was first detected in 2022 July with XMM-Newton observations, exhibiting an 18-minute period. The QPO frequency corresponds to coherent motion on scales $< 10r_g$, where r_g is the gravitational radius. The period decreased to 7.1 minutes over 2 yr, from 2022 July to 2024 March, with a decelerating period evolution. The QPO frequencies measured at the four epochs of XMM-Newton observations are $\nu = 0.93 \pm 0.06$ mHz (2022 July), $\nu = 1.67 \pm 0.04$ mHz (2023 February), $\nu = 2.21 \pm 0.05$ mHz (2023 August), $\nu = 2.35 \pm 0.05$ mHz (2024 March). The QPO frequency was found to be strongly correlated with the X-ray spectral slope Γ and the soft and hard X-ray fluxes. In addition, it was observed that the QPO is more prominently detected in the hard X-rays. The fractional rms of the QPO increases from 2%–7% in the 0.3–2 keV band to 15%–20% in the 2–10 keV band, across all observations. The origin of the QPO is still debated, but several models, such as stable mass transfer from a white dwarf companion, disk instabilities with a dependence on the accretion rate, or magnetoacoustic oscillations in a variable corona, have been extensively explored in Masterson et al. (2025).

Our second companion paper (E. T. Meyer et al. 2025) reports a new late-time radio flare in 1ES 1927+654, with a

³⁵ The Eddington ratio $\lambda_{\text{Edd}} = L_{\text{bol}}/L_{\text{Edd}}$ is the ratio between the measured bolometric luminosity L_{bol} and the Eddington luminosity L_{Edd} , where the latter is derived directly from the BH mass.

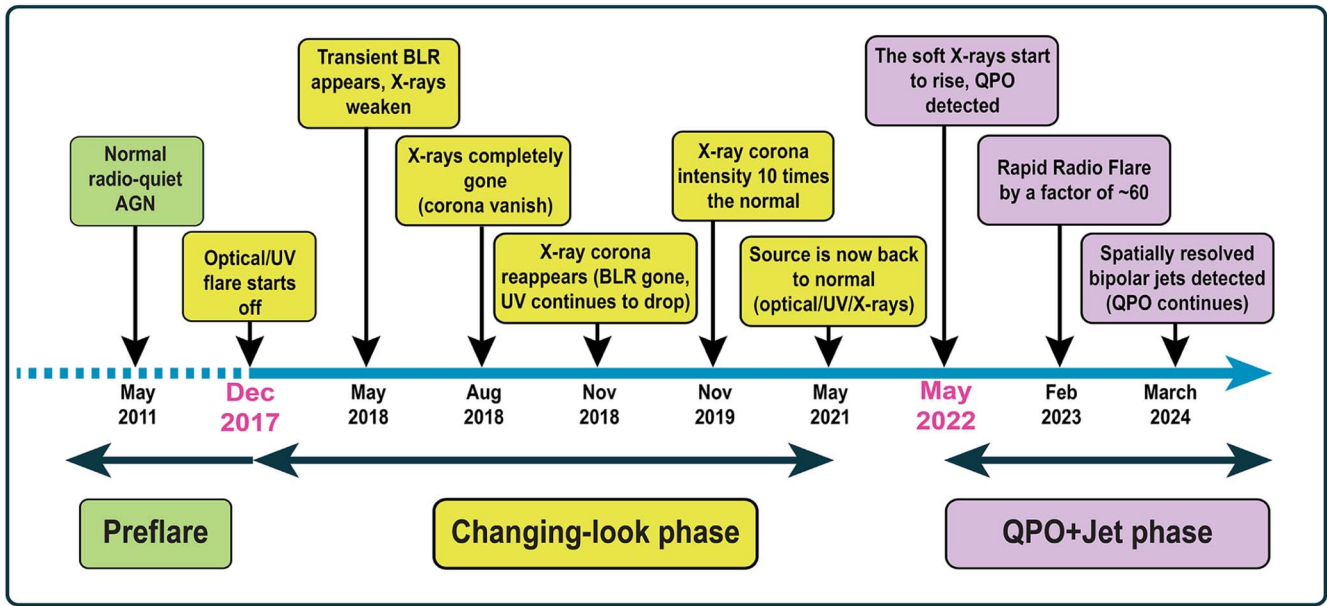


Figure 1. The timeline of the enigmatic behavior of the source 1ES 1927+654. From left to right are the three phases: the preflare phase (in green), the CL phase (in yellow), and the QPO+jet phase (in purple). The source exhibited typical radio-quiet Seyfert galaxy properties in radio, optical/UV, and X-rays until 2017 December, when there was a sudden flare in the optical/UV band, which reached a peak of ~ 100 times in ~ 3 months (B. Trakhtenbrot et al. 2019). A transient BLR also appeared during this time, while the X-rays start to weaken by 2018 May. This source never exhibited a BLR and was earlier classified as a true type 2 source, meaning that there was no line-of-sight obscuration in optical/UV/X-rays, yet there was no sign of a BLR emission. The X-ray coronal emission completely vanished in 2018 August (C. Ricci et al. 2020, 2021; S. Laha et al. 2022; M. Masterson et al. 2022), and it came back in 2018 October–November. By this time the BLR emission lines (broad Balmer lines) have disappeared, and the UV/optical flux continues to drop with a $\tau^{0.91}$ power-law decay. The X-ray corona revived and jumped to ~ 10 times that of preflare state in 2019 November, while the UV continued to drop. The source finally came back to its preflare state in 2021 May. Since 2022 May we have detected a gradual rise in soft X-rays and a QPO (Masterson et al. 2025, Nature, in press). Since 2023 February we have also detected a rapid radio flare, with a radio flux increase of ~ 60 times over a few months. The radio flux continues to stay in the high state for over the next year. Since 2024 March we have detected a spatially resolved bipolar jet in the K band, ~ 22 GHz (E. T. Meyer et al. 2025).

~ 40 - and 60 -fold increase in the core radio flux density at 5 and 8.4 GHz, respectively, over a short period of about 6 months starting in early 2023. The study also detected spatially resolved bipolar extensions of jets/outflows at 0.1 – 0.3 pc scales using VLBA observations. These outflows have been found to be mildly relativistic with a speed of $\sim 0.2c$. In Sections 3.1 and 3.2 of E. T. Meyer et al. (2025), we discuss the very long baseline interferometry (VLBI) resolution radio SED spanning from 2020 to 2024 January, along with core-subtracted K -band (23 GHz) VLBA images. These extended, resolved features provide clear evidence of a relativistic jet-driven outflow that is undergoing significant evolution, likely due to particle acceleration and shock interactions within the jet. The observed brightness temperature (T_b)³⁶ for the radio intensity values at 5 GHz, ranging from 10^7 to 10^9 K, indicates extremely high energy synchrotron-dominated emission. Such high brightness temperatures are typically associated with regions of intense, relativistic particle acceleration, suggesting that the emission is likely driven by a relativistic jet. Furthermore, it was observed that during the spectacular rise of the radio flare the higher-frequency X band (~ 8 GHz) became optically thin before the lower frequency band (~ 5 GHz), which is consistent with an optical depth from free-free absorption $\tau \propto \nu^{-2}$.

We have continued to follow up 1ES 1927+654 with observations from space-based and ground-based missions to track the multiwavelength evolution and the recent soft X-ray

³⁶ $T_b = \frac{4 \ln(2) c^2 S_\nu}{2 \pi k_B \theta_A \theta_B}$ K, where S_ν is the specific intensity over the solid angle and θ_A and θ_B are the full widths at half-power of the major and minor axes of an elliptical Gaussian beam, respectively.

rise, which we refer to as the “bright soft state” (R. Ghosh et al. 2023). In this paper we report the most recent multiwavelength observations of the source from Swift, XMM-Newton, NuSTAR, and the Zwicky Transient Facility (ZTF) from 2022 May to 2024 April. For clarity, in this paper we use “2018 flare” or “optical/UV flare” to indicate the original optical/UV outburst peaking in 2018, where the “preflare” (alternatively pre-CL) phase of the source indicates any time before 2017 (see Figure 1). The “post-flare” period indicates the period after 2022 January (when the high X-ray state first subsided), and the “radio flare” refers to the recent major increase in GHz radio flux that began in early 2023 (E. T. Meyer et al. 2025).

The paper is arranged as follows: Section 2 discusses the observation, data reduction, and analysis. Section 3 lists the most important results. Section 4 discusses the main scientific topics, and Section 5 lists the main conclusions.

2. Observations and Data Analysis

In this section, we discuss the X-ray, UV, and optical observations used in this work, which involves archival observations, as well as others obtained through the Director’s Discretionary Time (DDT) and Guest Investigator (GI) programs. Tables 1 and 2 list the observation details. For details of the radio data presented in this paper, see E. T. Meyer et al. (2025).

2.1. XMM-Newton

We have analyzed a total of nine XMM-Newton (F. Jansen et al. 2001) observations taken in 2011, 2022, 2023, and 2024 encompassing the pre-CL and the recent soft X-ray rise. The first 2011 May observation was taken during the pre-CL/

Table 1
The Details of Multiwavelength Observations of 1ES 1927+654 Used in This Work

Observation Band	Telescopes	Observation Date (YYYY-MM-DD)	Observation ID	Exposure (s)	Short-id
X-ray and UV	XMM-Newton	2011-05-20	671860201	28649	...
"	XMM-Newton	2022-07-26	902590201	27900	...
"	XMM-Newton	2022-07-28	902590301	19000	...
"	XMM-Newton	2022-07-30	902590401	19000	...
"	XMM-Newton	2022-08-01	902590501	22000	...
"	XMM-Newton	2023-02-21	915390701	34600	...
"	XMM-Newton	2023-08-07	931791401	36400	...
"	XMM-Newton	2024-03-04	932392001	33000	...
"	XMM-Newton	2024-03-12	932392101	33100	...
X-ray	NuSTAR	2023-05-27	80902632002	37117	...
"	NuSTAR	2023-06-26	80902632004	41074	...
"	NuSTAR	2023-08-05	80902632006	39840	...
"	NuSTAR	2023-09-03	80902632008	30987	...
X-ray and UV	Swift-XRT/UVOT	2018-05-17	00010682001	2190	S01
"	"	2023-05-09	00010682079	710	S79
"	"	2023-05-13	00010682080	885	S80
"	"	2023-05-17	00010682081	754	S81
"	"	2023-05-21	00010682082	887	S82
"	"	2023-05-20	00010682083	932	S83
"	"	2023-05-22	00010682084	993	S84
"	"	2023-05-23	00010682086	942	S86
"	"	2023-05-25	00010682087	436	S87
"	"	2023-05-26	00010682088	433	S88
"	"	2023-06-09	00010682089	1572	S89
"	"	2023-06-11	00010682090	953	S90
"	"	2023-06-12	00010682091	867	S91
"	"	2023-06-13	00010682092	872	S92
"	"	2023-06-15	00010682094	1624	S94
"	"	2023-06-17	00010682095	1654	S95
"	"	2023-06-21	00010682096	1424	S96
"	"	2023-06-24	00010682097	985	S97
"	"	2023-06-27	00010682098	827	S98
"	"	2023-07-03	00010682100	1008	S100
"	"	2023-07-06	00010682101	930	S101
"	"	2023-07-09	00010682102	907	S102
"	"	2023-07-15	00010682103	852	S103
"	"	2023-07-25	00010682104	366	S104
"	"	2023-07-27	00010682105	393	S105

Note. Refer to S. Laha et al. (2022) and R. Ghosh et al. (2023) for all the previous Swift observations.

preflare state of the source (see Table 1 and Figure 1 for details), the one in 2023 February (DDT; PI: S. Laha) was taken exactly when the source started to show signs of a radio burst, and the one in 2023 August (DDT; PI: S. Laha) was taken when the source has reached the radio-loud phase. The observations in 2024 March were obtained through DDT (PI: M. Masterson).

We used the latest XMM-Newton Science Analysis System (SAS v19.0.0) to process the Observation Data Files (ODFs) from all observations. For brevity we report only the European Photon Imaging Camera (EPIC-pn; L. Strüder et al. 2001) observations in this paper. The EVSELECT task was used to select the single and double events for the pn detector (PATTERN<4). We created light curves from the event files for each observation to account for the high background flaring using a rate cutoff of $<0.4 \text{ counts s}^{-1}$. We found significant particle background flares in the 2023 August observations but less in other epochs. We found that the 2023 February, 2023 August, and 2024 March observations show some pileup in the

soft X-rays (using the SAS task `epatplot`). For these observations we selected an annular region for source photons with inner and outer radii of $8''$ and $30''$, respectively, centered on the source. For the other observations the source regions were extracted from circular regions of $40''$ centered on the source. In all cases the background photons were extracted from appropriate regions away from the source but on the same CCD. The response matrices were generated using the SAS tasks `arfgen` and `rmfgen`. The spectra were grouped using the command `ftgrppha` with a minimum of 20 counts in each energy bin.

We analyzed the EPIC-pn spectra for the nine epochs separately using the phenomenological models (as per XSPEC notation) `tbabs*ztbabs*(powerlaw+bbbody)`. The blackbody component `bbbody` was required to model the soft X-ray excess (hereafter soft excess), while the `powerlaw` model is used to describe the Comptonized nonthermal spectrum from AGN corona. The `tbabs` model was used to describe the Galactic absorption, with a column density N_{H}

Table 2
The Details of Multiwavelength Observations of 1ES 1927+654 Used in This Work

Observation Band	Telescopes	Observation Date (YYYY-MM-DD)	Observation ID	Net Exposure (s)	Short-id
X-ray and UV	Swift-XRT/UVOT	2023-08-02	00010682106	822	S106
"	"	2023-08-05	00010682107	812	S107
"	"	2023-08-08	00010682108	750	S108
"	"	2023-08-11	00010682109	1012	S109
"	"	2023-08-14	00010682110	963	S110
"	"	2023-08-17	00010682111	872	S111
"	"	2023-08-26	00010682113	908	S113
"	"	2023-09-23	00010682115	850	S115
"	"	2023-09-27	00010682116	938	S116
"	"	2023-10-01	00010682117	1171	S117
"	"	2023-10-05	00010682118	807	S118
"	"	2023-10-09	00010682119	880	S119
"	"	2023-10-13	00010682120	948	S120
"	"	2023-10-17	00010682121	920	S121
"	"	2023-10-21	00010682122	862	S122
"	"	2023-10-24	00010682123	867	S123
"	"	2023-11-06	00010682124	687	S124
"	"	2023-11-10	00010682125	842	S125
"	"	2023-11-15	00010682126	717	S126
"	"	2023-11-18	00010682127	868	S127
"	"	2023-11-22	00010682128	935	S128
"	"	2023-11-26	00010682129	1096	S129
"	"	2023-11-30	00010682130	1045	S130
"	"	2023-12-04	00010682131	1278	S131
"	"	2023-12-08	00010682132	892	S132
"	"	2023-12-13	00010682133	557	S133
"	"	2023-12-25	00010682134	883	S134
"	"	2023-12-28	00010682135	933	S135
"	"	2024-01-05	00010682137	933	S137
"	"	2024-01-09	00010682138	852	S138
"	"	2024-01-13	00010682139	908	S139
"	"	2024-01-17	00010682140	996	S140
"	"	2024-01-24	00097196023	797	S140A
"	"	2024-02-03	00097196024	847	S140B
"	"	2024-02-21	00097196025	872	S140C
"	"	2024-02-28	00010682141	960	S141
"	"	2024-03-10	00097196027	1020	S141A
"	"	2024-04-06	00016519001	847	S143
"	"	2024-04-11	00016519002	900	S144A

held fixed to $6.42 \times 10^{20} \text{ cm}^{-2}$ (P. M. W. Kalberla et al. 2005). The `ztbabs` model was used to describe the host galaxy intrinsic absorption, with a best-fit column density $N_{\text{H}} \sim (4-5) \times 10^{20} \text{ cm}^{-2}$. This low level of intrinsic absorption has been present since the pre-CL state (in 2011), indicating a large-scale absorber, possibly galactic dust lanes (see, e.g., S. Laha et al. 2020). We have also used two Gaussian profiles to model the narrow emission lines at ~ 0.56 and ~ 1 keV in the soft X-ray 0.3–2 keV spectra. To accurately constrain and characterize the narrow emission lines in the soft X-rays, we require a simultaneous spectral fit of EPIC-pn and the high-resolution Reflection Grating Spectrometer (RGS). This is beyond the scope of this paper, and therefore we defer the study of the emission lines to a future work. The best-fit continuum parameters are reported in Table 3.

2.2. Swift

2.2.1. Swift-XRT and UVOT

1ES 1927+654 was observed by the Neil Gehrels Swift Observatory X-ray Telescope (XRT; D. N. Burrows et al.

2005) initially on a monthly cadence from 2022 January to November, and then at a weekly and biweekly cadence from 2022 December to 2024 May (see Tables 1 and 2) under the DDT and Swift-GI programs (PI: S. Laha). We use abbreviations for the Swift observations to easily identify them. The names begin with the letter ‘‘S’’ and have been used in our earlier works (S. Laha et al. 2022; R. Ghosh et al. 2023). The observations up to S78 (2018–2022 May) have been reported in our previous works (S. Laha et al. 2022; R. Ghosh et al. 2023). In this paper we discuss only the observations from 2022 May to 2024 April (S79–S144A).

We followed the automated XRT analysis approach via the online tools³⁷ (P. A. Evans et al. 2009) for the XRT data in all our observations as recommended for point sources by the Swift help desk. We used similar spectral models to fit the XRT spectra to those that have been used in XMM-Newton observations (see Tables 4 and 5). We note here that because of the poor statistical quality of the XRT spectra, mostly due to

³⁷ <https://www.swift.ac.uk/user-objects>

Table 3
The Best-fit Parameters Obtained from Fitting the XMM-Newton EPIC-pn Observations

Models	Parameter	20/05/11	26/07/22	28/07/22	30/07/22	01/08/22	21/02/23	07/08/23	04/03/24	12/03/24
Gal. abs.	$N_{\text{H}} (\times 10^{20})$	6.4 (f)	6.4 (f)	6.4 (f)	6.4 (f)					
ztbabs	$N_{\text{H}} (\times 10^{20})$	$4.04^{+0.53}_{-0.52}$	$3.22^{+0.70}_{-0.67}$	$2.39^{+0.65}_{-0.64}$	$2.11^{+0.68}_{-0.69}$	$1.02^{+0.86}_{-1.08}$	$4.69^{+0.56}_{-0.56}$	$5.60^{+0.52}_{-0.52}$	$5.91^{+0.64}_{-0.64}$	$5.76^{+0.55}_{-0.54}$
blackbody	$T_{\text{in}} (\text{keV})$	$0.16^{+0.01}_{-0.01}$	$0.15^{+0.01}_{-0.01}$	$0.15^{+0.01}_{-0.01}$	$0.14^{+0.01}_{-0.01}$	$0.15^{+0.01}_{-0.01}$	$0.14^{+0.01}_{-0.02}$	$0.14^{+0.01}_{-0.01}$	$0.15^{+0.01}_{-0.01}$	$0.15^{+0.02}_{-0.02}$
	norm (10^{-4})	$0.39^{+0.04}_{-0.03}$	$0.72^{+0.12}_{-0.09}$	$0.66^{+0.10}_{-0.08}$	$0.61^{+0.08}_{-0.07}$	$0.79^{+0.10}_{-0.09}$	$2.97^{+0.17}_{-0.16}$	$4.88^{+0.18}_{-0.17}$	$5.59^{+0.22}_{-0.21}$	$5.39^{+0.18}_{-0.17}$
powerlaw	Γ	$2.45^{+0.04}_{-0.04}$	$2.65^{+0.04}_{-0.04}$	$2.70^{+0.04}_{-0.04}$	$2.71^{+0.04}_{-0.04}$	$2.48^{+0.06}_{-0.07}$	$3.10^{+0.04}_{-0.04}$	$3.21^{+0.04}_{-0.04}$	$3.26^{+0.05}_{-0.05}$	$3.27^{+0.04}_{-0.04}$
	norm (10^{-2})	$0.28^{+0.01}_{-0.01}$	$0.45^{+0.02}_{-0.02}$	$0.49^{+0.02}_{-0.02}$	$0.51^{+0.02}_{-0.02}$	$0.42^{+0.02}_{-0.03}$	$1.07^{+0.05}_{-0.05}$	$1.36^{+0.06}_{-0.05}$	$1.49^{+0.07}_{-0.07}$	$1.45^{+0.06}_{-0.06}$
	χ^2/dof	688/695	751/762	643/624	588/639	929/950	607/632	657/652	623/626	733/680
	$L_{(0.3-2)}^{\text{bb}}$ keV (10^{42})	$2.18^{+0.11}_{-0.11}$	$2.41^{+0.22}_{-0.22}$	$2.46^{+0.22}_{-0.22}$	$2.59^{+0.20}_{-0.20}$	$2.95^{+0.21}_{-0.20}$	$13.06^{+0.43}_{-0.43}$	$21.74^{+0.49}_{-0.49}$	$25.94^{+0.62}_{-0.61}$	$25.06^{+0.50}_{-0.50}$
	$L_{(2-10)}^{\text{pow}}$ keV (10^{42})	$2.45^{+0.03}_{-0.03}$	$2.89^{+0.03}_{-0.03}$	$3.01^{+0.03}_{-0.03}$	$3.11^{+0.04}_{-0.04}$	$3.33^{+0.04}_{-0.04}$	$3.95^{+0.05}_{-0.05}$	$4.35^{+0.05}_{-0.05}$	$4.48^{+0.06}_{-0.06}$	$4.29^{+0.05}_{-0.05}$

Note. The unabsorbed soft X-ray blackbody (0.3–2 keV) and power-law (2–10 keV) luminosities, denoted by $L_{(0.3-2)}^{\text{bb}}$ keV and $L_{(2-10)}^{\text{pow}}$ keV, respectively, are in the units of erg s^{-1} .

the low effective area and low exposure times per snapshot (300–800 s), resulting in low count rate $\sim 0.8 \text{ counts s}^{-1}$ (compared to $\sim 15 \text{ counts s}^{-1}$ in XMM-Newton), we did not statistically require the intrinsic absorber model component (ztbabs), which was needed in the XMM-Newton spectral fit. In other words, we did not find any improvement in fit statistics ($\Delta\chi^2 = 0$) on addition of this model in the XRT spectra. Not being able to model the intrinsic absorption with the XRT spectra results in a slightly lower estimation of the intrinsic soft X-ray 0.3–2 keV flux by 15%–20% compared to XMM-Newton, but the 2–10 keV flux remains unaffected.

Swift-UVOT (P. W. A. Roming et al. 2005) observed the source simultaneously along with Swift-XRT. Refer to R. Ghosh et al. (2023) for a full description of UVOT data reprocessing and analysis, which we follow here. The UV flux densities were corrected for Galactic absorption using the correction magnitude of $A_{\lambda} = 0.690$ obtained from the NASA Extragalactic Database (NED).³⁸ Figure 2 shows the X-ray flux and UV flux density light curves as measured by Swift.

We estimated the Eddington ratio of the source, as on 2024 April, using the relation $\lambda_{\text{Edd}} = L_{\text{bol}}/L_{\text{Edd}}$, where L_{Edd} is the Eddington luminosity of the source, assuming a black hole (BH) of mass $\sim 10^6 M_{\odot}$ (R. Li et al. 2022). To estimate L_{bol} , we have used the integrated UV luminosity in the band 0.001–100 eV and the X-ray luminosity in the band 0.3–10 keV, obtained by fitting the Swift-UVOT photometric data simultaneously with the XRT spectrum (see R. Ghosh et al. 2023 for details). We estimate an Eddington ratio of $\lambda_{\text{Edd}} \sim 0.3$. Considering a 2–10 keV luminosity of $4 \times 10^{42} \text{ erg s}^{-1}$, this would give us a bolometric correction of $\kappa \sim L_{\text{bol}}/L_{2-10 \text{ keV}} \sim 10$, consistent with typical sub-Eddington AGN (R. V. Vasudevan & A. C. Fabian 2007).

2.3. NuSTAR

1ES 1927+654 has been observed by NuSTAR four times in 2023 (GI program; PI: S. Laha) when the source was getting radio bright, capturing the hard X-ray spectra during the radio rise. The data were processed using the NuSTAR Data Analysis Software (NUSTARDAS) version 2.1.2. Calibration of the raw event files was performed using the *nupipeline* script and the response file from NuSTAR Calibration Database (CALDB)

version 20211020. The source and background spectra are extracted from 30'' ($\approx 50\%$ of the encircled energy fraction at 10 keV) and 50'' circular regions, respectively. The *nuproducts* scripts are used to generate the source and background spectra files, along with response matrix files and ancillary response files. Finally, using *grppha*, the NuSTAR spectra are grouped with at least 20 counts bin^{-1} in order to use the χ^2 statistics.

Figure 3 shows the four epochs of NuSTAR spectra along with the XMM-Newton spectra in 2023. The NuSTAR 3–40 keV spectra are well described by a simple power law with a slope $\Gamma \sim 3.2$, consistent with the four observations (and also consistent with XMM-Newton observations during similar epochs). See Table 6 for the best-fit parameters and flux values.

2.4. Zwicky Transient Facility

We obtained the ZTF optical photometric data for 1ES 1927+654 for the period from 2018 January to 2024 March through the public release website DR 21³⁹ (E. C. Bellm et al. 2019; M. J. Graham et al. 2019). The ZTF survey covers the visible northern sky, reaching median depths of approximately 20.8 mag in the *g* band and 20.6 mag in the *r* band (AB, 5σ) with 30 s exposures. It utilizes point-spread function fitting for photometry to construct light curves. We plot the ZTF optical *r*-band light curve of 1ES 1927+654, roughly at a daily cadence containing observations until 2024 March 1, in Figure 2. Note that the host galaxy contribution is not subtracted from the *r*-band flux.

2.5. Fermi-LAT

The Fermi-LAT gamma-ray observatory, launched in 2008, is sensitive to photons in the energy range of $\sim 30 \text{ MeV}$ –300 GeV and mostly operates in a sky-scanning mode that has produced a deep archive of gamma-monitoring data covering the past 16 yr (S. Abdollahi et al. 2020).

Fermi-LAT event and spacecraft data were extracted using a 15° region of interest, an energy range of 100 MeV–300 GeV, a zenith angle cut of 90° , and the recommended event class and type for point-source analysis. The time cuts of the collected data included the entire Fermi mission runtime, which corresponds to a mission elapsed time (MET) range of 239557417–741587557. The analysis was performed using the publicly available

³⁸ <https://ned.ipac.caltech.edu>

³⁹ <https://www.ztf.caltech.edu/ztf-public-releases.html>

Table 4
The Spectral Parameters Obtained Using Swift and XMM-Newton UV and X-ray Observations of 1ES 1927+654

ID(DD/ MM/YY)	$F_{0.3-2}$ keV ^a	F_{2-10} keV ^a	$F_{1.5-2.5}$ keV ^a	kT (keV)	Γ	UV Filter	UV Flux Density ^b	α_{OX}	χ^2/χ^2_{ν}
X1 (20/05/11)	9.41 ± 0.66	3.92 ± 0.08	1.64 ± 0.02	0.20 ± 0.01	2.21 ^{+0.02} _{-0.02}	UVM2	1.34 ± 0.03	0.918	185/1.37
S79 (09/05/23)	47.98 ± 4.39	7.34 ± 2.40	5.50 ± 0.84	0.23 ± 0.06	2.82 ^{+0.32} _{-0.28}	UVW2	2.17 ± 0.12	0.883	61.88/0.73
S80 (13/05/23)	40.79 ± 4.18	11.79 ± 3.99	4.91 ± 0.88	0.13 ± 0.04	2.42 ^{+0.50} _{-0.61}	UVW2	2.02 ± 0.11	0.890	70.32/1.00
S81 (17/05/23)	47.25 ± 4.48	8.18 ± 2.75	5.23 ± 0.72	0.20 ± 0.04	2.65 ^{+0.29} _{-0.37}	UVW2	2.29 ± 0.11	0.901	52.35/0.77
S82 (21/05/23)	40.30 ± 3.86	5.09 ± 2.05	3.63 ± 0.88	0.19 ± 0.03	2.67 ^{+0.38} _{-0.54}	UVW2	1.96 ± 0.11	0.936	73.22/1.05
S83 (20/05/23)	32.15 ± 2.40	8.74 ± 1.85	4.03 ± 0.38	0.17 ± 0.03	2.35 ^{+0.23} _{-0.27}	UVW2	1.82 ± 0.12	0.934	76.65/0.72
S84 (22/05/23)	47.78 ± 4.43	6.00 ± 1.95	4.81 ± 0.66	0.22 ± 0.05	2.90 ^{+0.30} _{-0.30}	UVW2	2.05 ± 0.11	0.896	92.00/1.15
S86 (23/05/23)	49.47 ± 7.17	5.25 ± 2.47	4.26 ± 0.82	0.20 ± 0.06	2.96 ^{+0.64} _{-0.75}	UVW2	2.20 ± 0.16	0.928	27.88/0.59
S87 (25/05/23)	51.18 ± 5.12	9.86 ± 3.13	5.63 ± 0.76	0.18 ± 0.05	2.64 ^{+0.29} _{-0.40}	UVW2	1.81 ± 0.13	0.849	50.49/0.78
S88 (26/05/23)	48.63 ± 6.83	5.02 ± 2.04	5.75 ± 1.48	0.29 ± 0.08	3.14 ^{+0.46} _{-0.47}	UVW2	1.76 ± 0.13	0.841	57.01/1.24
S89 (09/06/23)	45.36 ± 2.95	7.43 ± 1.95	4.21 ± 0.42	0.18 ± 0.02	2.45 ^{+0.28} _{-0.38}	UVW2	1.96 ± 0.11	0.911	100.76/ 0.87
S90 (11/06/23)	44.17 ± 4.22	21.93 ± 11.75	4.42 ± 0.79	0.16 ± 0.02	1.92 ^{+0.39} _{-0.49}	UVW2	2.05 ± 0.11	0.910	48.38/0.78
S91 (12/06/23)	45.29 ± 4.62	8.07 ± 3.94	4.30 ± 0.77	0.17 ± 0.03	2.46 ^{+0.58} _{-0.69}	UVW2	2.05 ± 0.11	0.912	47.20/0.76
S92 (13/06/23)	50.97 ± 4.68	9.54 ± 3.01	5.03 ± 0.68	0.17 ± 0.03	2.49 ^{+0.32} _{-0.46}	UVW2	2.02 ± 0.11	0.886	67.84/0.92
S94 (15/06/23)	45.28 ± 2.71	8.60 ± 1.79	4.58 ± 0.40	0.17 ± 0.02	2.53 ^{+0.21} _{-0.27}	UVW2	2.00 ± 0.11	0.900	113.26/ 0.83
S95 (17/06/23)	47.88 ± 2.82	7.30 ± 1.70	4.26 ± 0.38	0.18 ± 0.02	2.46 ^{+0.25} _{-0.32}	UVW2	1.94 ± 0.12	0.907	100.74/ 0.79
S96 (21/06/23)	48.16 ± 4.10	5.37 ± 1.64	4.06 ± 0.52	0.19 ± 0.04	2.95 ^{+0.25} _{-0.27}	UVW2	2.17 ± 0.13	0.934	80.38/0.90
S97 (24/06/23)	43.41 ± 3.64	6.99 ± 2.217	4.42 ± 0.54	0.19 ± 0.04	2.70 ^{+0.26} _{-0.33}	UVW2	1.92 ± 0.11	0.899	55.14/0.63
S98 (27/06/23)	52.34 ± 4.77	5.81 ± 1.91	5.33 ± 0.87	0.23 ± 0.05	2.93 ^{+0.33} _{-0.31}	UVW2	1.96 ± 0.11	0.872	63.01/0.77
S100 (03/07/23)	47.17 ± 3.96	5.25 ± 1.73	3.93 ± 0.55	0.19 ± 0.04	2.91 ^{+0.28} _{-0.31}	UVW2	2.15 ± 0.13	0.938	55.61/0.67
S101 (06/07/23)	47.61 ± 3.86	9.38 ± 3.72	3.91 ± 0.56	0.17 ± 0.01	2.07 ^{+0.54} _{-0.68}	UVW2	2.05 ± 0.11	0.931	70.60/0.89
S102 (09/07/23)	44.35 ± 3.49	8.59 ± 3.22	4.20 ± 0.62	0.17 ± 0.02	2.38 ^{+0.40} _{-0.67}	UVW2	2.09 ± 0.11	0.922	75.05/0.83
S103 (15/07/23)	47.51 ± 4.03	7.85 ± 2.39	4.90 ± 0.62	0.19 ± 0.03	2.61 ^{+0.28} _{-0.35}	UVW2	2.29 ± 0.13	0.911	77.34/0.94
S104 (25/07/23)	47.61 ± 3.86	9.38 ± 3.72	3.91 ± 0.56	0.17 ± 0.10	2.69 ^{+0.32} _{-0.59}	UVW2	2.26 ± 0.18	0.905	38.51/0.77
S105 (27/07/23)	46.23 ± 5.70	14.58 ± 9.48	5.51 ± 1.15	0.18 ± 0.03	1.91 ^{+0.76} _{-0.68}	UVW2	2.07 ± 0.14	0.875	42.19/0.98
S106 (02/08/23)	60.17 ± 5.24	7.85 ± 2.50	6.19 ± 0.87	0.21 ± 0.04	2.80 ^{+0.28} _{-0.30}	UVW2	2.09 ± 0.14	0.857	65.07/0.79
S107 (05/08/23)	41.35 ± 3.39	8.83 ± 2.53	4.00 ± 0.49	0.16 ± 0.02	2.31 ^{+0.33} _{-0.40}	UVW2	2.11 ± 0.15	0.932	87.54/0.97
S108 (08/08/23)	49.76 ± 4.70	8.04 ± 2.85	5.29 ± 0.83	0.20 ± 0.07	2.72 ^{+0.33} _{-0.36}	UVW2	1.91 ± 0.12	0.868	56.44/0.81
S109 (11/08/23)	50.12 ± 3.95	6.19 ± 2.18	4.09 ± 0.54	0.18 ± 0.03	2.70 ^{+0.31} _{-0.42}	UVW2	1.89 ± 0.09 ⁺	0.910	68.30/0.77
S110 (14/08/23)	60.79 ± 5.63	7.12 ± 2.58	5.43 ± 0.76	0.20 ± 0.05	2.96 ^{+0.32} _{-0.33}	UVW2	2.07 ± 0.14 ⁺	0.892	60.05/0.77
S111 (17/08/23)	50.15 ± 4.08	9.45 ± 3.52	4.51 ± 0.65	0.17 ± 0.02	2.32 ^{+0.42} _{-0.63}	UVW2	2.02 ± 0.11 ⁺	0.904	69.34/0.83
S113 (26/08/23)	44.67 ± 3.92	7.74 ± 2.76	4.38 ± 0.62	0.17 ± 0.03	2.59 ^{+0.34} _{-0.47}	UVW2	1.91 ± 0.12 ⁺	0.900	83.81/1.03
S115 (23/09/23)	56.49 ± 4.74	9.78 ± 2.81	5.21 ± 0.72	0.18 ± 0.05	2.27 ^{+0.39} _{-0.55}	UVW2	1.68 ± 0.09 ⁺	0.845	49.81/0.66
S116 (27/09/23)	54.52 ± 4.73	12.06 ± 3.97	6.39 ± 0.83	0.18 ± 0.05	2.52 ^{+0.30} _{-0.40}	UVW2	1.59 ± 0.04 ⁺	0.806	72.23/0.90
S117 (01/10/23)	46.85 ± 2.98	9.96 ± 2.49	5.12 ± 0.50	0.19 ± 0.02	2.18 ^{+0.30} _{-0.41}	UVW2	2.31 ± 0.15 ⁺	0.906	92.11/0.77
S118 (05/10/23)	44.67 ± 3.92	7.74 ± 2.76	4.38 ± 0.62	0.19 ± 0.05	2.56 ^{+0.27} _{-0.32}	UVW2	1.17 ± 0.09 ⁺	0.769	80.79/0.94
S119 (09/10/23)	58.67 ± 5.48	4.13 ± 2.16	5.00 ± 0.91	0.22 ± 0.03	3.09 ^{+0.48} _{-0.41}	UVW2	1.74 ± 0.10 ⁺	0.862	69.78/0.88
S120 (13/10/23)	58.64 ± 4.37	8.14 ± 2.32	6.45 ± 0.85	0.22 ± 0.04	2.78 ^{+0.26} _{-0.27}	UVW2	78.63/0.76
S121 (17/10/23)	53.42 ± 4.20	10.73 ± 3.81	5.75 ± 0.71	0.19 ± 0.03	2.40 ^{+0.35} _{-0.57}	UVW2	1.57 ± 0.10 ⁺	0.822	80.18/0.86
S122 (21/10/23)	54.63 ± 4.47	9.54 ± 3.31	5.88 ± 0.72	0.19 ± 0.06	2.69 ^{+0.31} _{-0.37}	UVW2	1.55 ± 0.10 ⁺	0.816	87.44/0.96

Notes. For comparison with the preflare values, we keep the XMM-Newton observation.

The UV flux density was corrected for Galactic absorption using the correction magnitude of $A_{\lambda} = 0.690$ obtained from NED.

^a Flux in units of 10^{-12} erg cm⁻² s⁻¹ corrected for Galactic absorption.

^b UV flux density in units of 10^{-15} erg cm⁻² s⁻¹ Å⁻¹ and $\alpha_{\text{OX}} = -0.385 \log(F_{2 \text{ keV}}/F_{2500\text{\AA}})$

easyFermi, which processes the user-provided data files to perform a Fermi-LAT binned likelihood analysis following the standard methodology. The easyFermi analysis was performed over a time range from 2024 January 1 at 12 a.m. to 2024 June 1 at 12 a.m., corresponding to an MET range of 725760001–738892801. The galactic model `gll_iem_v07.fits` and the isotropic diffuse emission model `iso_P8R3_SOURCE_V3_v1.txt` were used for the analysis. To

obtain a converged fit, a free source radius of 10° was used with only the normalization free.

We produced a light curve with 20 time bins over the above MET range. Based on the values of the test statistic (TS)⁴⁰ for the light-curve periods, at no time period is the source

⁴⁰ The TS is a maximum likelihood method commonly used as a Fermi data analysis tool to determine whether a source is detected or not.

Table 5
The Spectral Parameters Obtained Using Swift UV and X-ray Observations of 1ES 1927+654

ID(DD/MM/YY)	$F_{0.3-2}$ keV ^a	F_{2-10} keV ^a	$F_{1.5-2.5}$ keV ^a	kT (keV)	Γ	UV Filter	UV Flux Density ^b	α_{OX}	χ^2/χ^2_{ν}
X1 (20/05/11)	9.41 ± 0.66	3.92 ± 0.08	1.64 ± 0.02	0.20 ± 0.01	2.21 ^{+0.02} _{-0.02}	UVM2	1.34 ± 0.03	0.918	185/1.37
S123 (24/10/23)	52.45 ± 4.47	9.92 ± 2.85	5.67 ± 0.67	0.18 ± 0.04	2.58 ^{+0.28} _{-0.37}	UVW2	1.68 ± 0.10 [†]	0.835	71.72/0.82
S124 (06/11/23)	49.06 ± 6.18	10.97 ± 5.32	5.21 ± 0.93	0.17 ± 0.04	2.32 ^{+0.54} _{-0.77}	UVW2	1.74 ± 0.10 [†]	0.855	26.66/0.67
S125 (10/11/23)	45.21 ± 4.36	11.53 ± 4.00	5.88 ± 0.80	0.19 ± 0.05	2.40 ^{+0.32} _{-0.47}	UVW2	2.35 ± 0.13	0.885	66.76/0.95
S126 (15/11/23)	53.16 ± 4.58	7.40 ± 3.29	4.16 ± 0.64	0.17 ± 0.02	2.37 ^{+0.56} _{-0.72}	UVW2	64.64/0.82
S127 (18/11/23)	47.85 ± 4.05	12.62 ± 3.73	5.72 ± 0.68	0.18 ± 0.03	2.28 ^{+0.33} _{-0.45}	UVW2	1.65 ± 0.10 [†]	0.831	90.42/1.06
S128 (22/11/23)	58.52 ± 4.39	10.88 ± 2.86	5.75 ± 0.70	0.16 ± 0.03	2.57 ^{+0.27} _{-0.36}	UVW2	1.72 ± 0.09 [†]	0.837	68.23/0.69
S129 (26/11/23)	54.03 ± 5.47	9.52 ± 3.52	5.08 ± 0.77	0.17 ± 0.02	2.45 ^{+0.35} _{-0.51}	UVW2	1.39 ± 0.08 [†]	0.822	49.59/0.86
S130 (30/11/23)	47.57 ± 4.40	13.43 ± 5.64	5.33 ± 0.78	0.18 ± 0.02	1.97 ^{+0.54} _{-0.59}	UVW2	2.26 ± 0.13 [†]	0.895	61.67/0.87
S131 (04/12/23)	54.79 ± 3.34	7.85 ± 1.80	5.72 ± 0.56	0.21 ± 0.03	2.71 ^{+0.22} _{-0.19}	UVW2	1.57 ± 0.11 [†]	0.823	116.26/ 0.89
S132 (08/12/23)	53.56 ± 4.22	12.08 ± 3.01	6.15 ± 0.66	0.18 ± 0.02	2.38 ^{+0.26} _{-0.35}	UVW2	1.59 ± 0.10 [†]	0.813	95.73/0.85
S133 (13/12/23)	59.10 ± 5.57	9.34 ± 4.00	5.75 ± 0.71	0.17 ± 0.02	2.46 ^{+0.38} _{-0.53}	UVW2	1.54 ± 0.10 [†]	0.819	48.32/0.76
S134 (25/12/23)	56.98 ± 4.01	7.81 ± 2.00	5.52 ± 0.59	0.20 ± 0.03	2.74 ^{+0.21} _{-0.24}	UVW2	1.72 ± 0.10 [†]	0.844	100.93/ 0.91
S135 (28/12/23)	51.02 ± 4.14	8.10 ± 2.89	5.08 ± 0.69	0.20 ± 0.02	2.35 ^{+0.37} _{-0.58}	UVW2	1.62 ± 0.09 [†]	0.848	76.28/0.90
S137 (05/01/24)	55.71 ± 4.86	8.77 ± 2.80	6.81 ± 1.07	0.22 ± 0.04	2.64 ^{+0.31} _{-0.38}	UVW2	1.15 ± 0.09 [†]	0.742	68.78/0.83
S138 (09/01/24)	54.95 ± 4.91	7.72 ± 2.80	5.45 ± 0.76	0.20 ± 0.03	2.62 ^{+0.35} _{-0.50}	UVW2	1.60 ± 0.09 [†]	0.834	62.49/0.81
S139 (13/01/24)	54.46 ± 4.16	10.68 ± 3.89	5.88 ± 0.68	0.18 ± 0.03	2.50 ^{+0.28} _{-0.39}	UVW2	1.31 ± 0.09 [†]	0.788	90.08/0.93
S140 (17/01/24)	64.76 ± 5.17	9.72 ± 3.03	6.66 ± 0.81	0.20 ± 0.05	2.78 ^{+0.26} _{-0.30}	UVW2	1.24 ± 0.09 [†]	0.758	80.64/0.82
S140A (24/01/24)	52.36 ± 5.00	9.31 ± 3.09	5.80 ± 0.82	0.20 ± 0.03	2.40 ^{+0.48} _{-0.33}	UVW2	1.91 ± 0.11	0.853	75.16/1.03
S140B (03/02/24)	52.97 ± 4.33	16.78 ± 7.31	6.50 ± 0.92	0.20 ± 0.03	1.94 ^{+0.67} _{-0.87}	UVW2	1.68 ± 0.11	0.813	63.6/0.79
S140C (21/02/24)	61.15 ± 4.97	9.69 ± 3.00	6.66 ± 0.81	0.19 ± 0.04	2.70 ^{+0.27} _{-0.35}	UVW2	1.91 ± 0.10	0.830	83.13/0.98
S141 (28/02/24)	62.76 ± 7.15	7.52 ± 3.64	5.63 ± 1.04	0.19 ± 0.04	2.78 ^{+0.44} _{-0.57}	UVW2	2.00 ± 0.11	0.866	40.88/0.83
S141A (10/03/24)	63.39 ± 7.15	9.78 ± 2.61	6.51 ± 0.68	0.20 ± 0.03	2.66 ^{+0.23} _{-0.28}	UVW2	1.81 ± 0.13	0.855	90.03/0.77
S143 (06/04/24)	74.7 ± 4.96	9.71 ± 2.67	6.08 ± 0.78	0.20 ± 0.05	2.81 ^{+0.24} _{-0.30}	UVW2	2.15 ± 0.13	0.865	89.82/0.92
S144A (11/04/24)	54.71 ± 5.20	13.79 ± 5.82	5.18 ± 0.75	0.17 ± 0.02	1.93 ^{+0.76} _{-0.96}	UVW2	2.02 ± 0.11	0.881	64.06/0.79

Notes. The UV flux density was corrected for Galactic absorption using the correction magnitude of $A_{\lambda} = 0.690$ obtained from NED.

^a Flux in units of 10^{-12} erg cm^{-2} s^{-1} corrected for Galactic absorption.

^b UV flux density in units of 10^{-15} erg cm^{-2} s^{-1} \AA^{-1} and $\alpha_{\text{OX}} = -0.385 \log(F_{2 \text{ keV}}/F_{2500\text{\AA}})$

significantly detected, with the highest TS being 0.665, associated with an MET range of 733639750–734296390. No detectable flare was measured in the Fermi data during the analysis time period.

In addition to the above analysis, we also produced a light curve for the position of 1ES 1927+654 in a similar way for the entire operating time of Fermi through early 2024 with a 6-month time binning. Again, no significant detection was made at any time, with the highest value of the TS ~ 4 (likely a background or nearby source fluctuation) and the vast majority consistent with zero.

3. Results

We summarize the multiwavelength results from our campaign during the period 2022 May–2024 April. The XMM-Newton and NuSTAR X-ray observations were coordinated to cover the time period of the radio flare (2023 February–August). The left panel of Figure 3 shows the time stamps when the X-ray observations were made covering the radio flare phase. The right panel of Figure 3 shows the XMM-Newton and NuSTAR spectral overplots covering this time period. The NuSTAR spectra in blue do not show any variation in slope or flux at $<5\%$ during the ~ 60 times radio flux rise. See Tables 3 and 6 for details.

In this section we clearly make a distinction between the two quantities: the soft excess and the soft X-ray fluxes. The former is the “excess” in the 0.3–2 keV flux after fitting a power-law continuum, and we have used a blackbody model to describe it. The latter, on the other hand, refers to the total flux in the 0.3–2 keV band, including contributions from both the power law and the blackbody. We note that the soft excess contributes to $\sim 30\%$ – 40% of the soft X-ray flux.

3.1. The X-Ray Light-curve Evolution

Both the soft X-ray (0.3–2 keV) flux and hard X-ray (2–10 keV) flux of 1ES 1927+654 have shown notable variability on timescales of weeks to months in the 2022 May–2024 April period. As previously reported in R. Ghosh et al. (2023), the Swift-XRT observations of 2022 May 20 showed that the 0.3–2 keV and 2–10 keV fluxes had reached their preflare values of $\sim 4 \times 10^{-12}$ erg cm^{-2} s^{-1} and $\sim 9 \times 10^{-12}$ erg cm^{-2} s^{-1} , respectively. As shown in Figure 2 and Tables 4 and 5, the soft X-ray flux has since risen steadily over the past 2 yr. As of 2024 April 11, the soft X-ray flux level is ~ 8 times that of its preflare value. On the other hand, the 2–10 keV light curve exhibits stochastic variations (<2 times) with a slow steady rise. These estimates are also corroborated by XMM-Newton observations during this time period (see

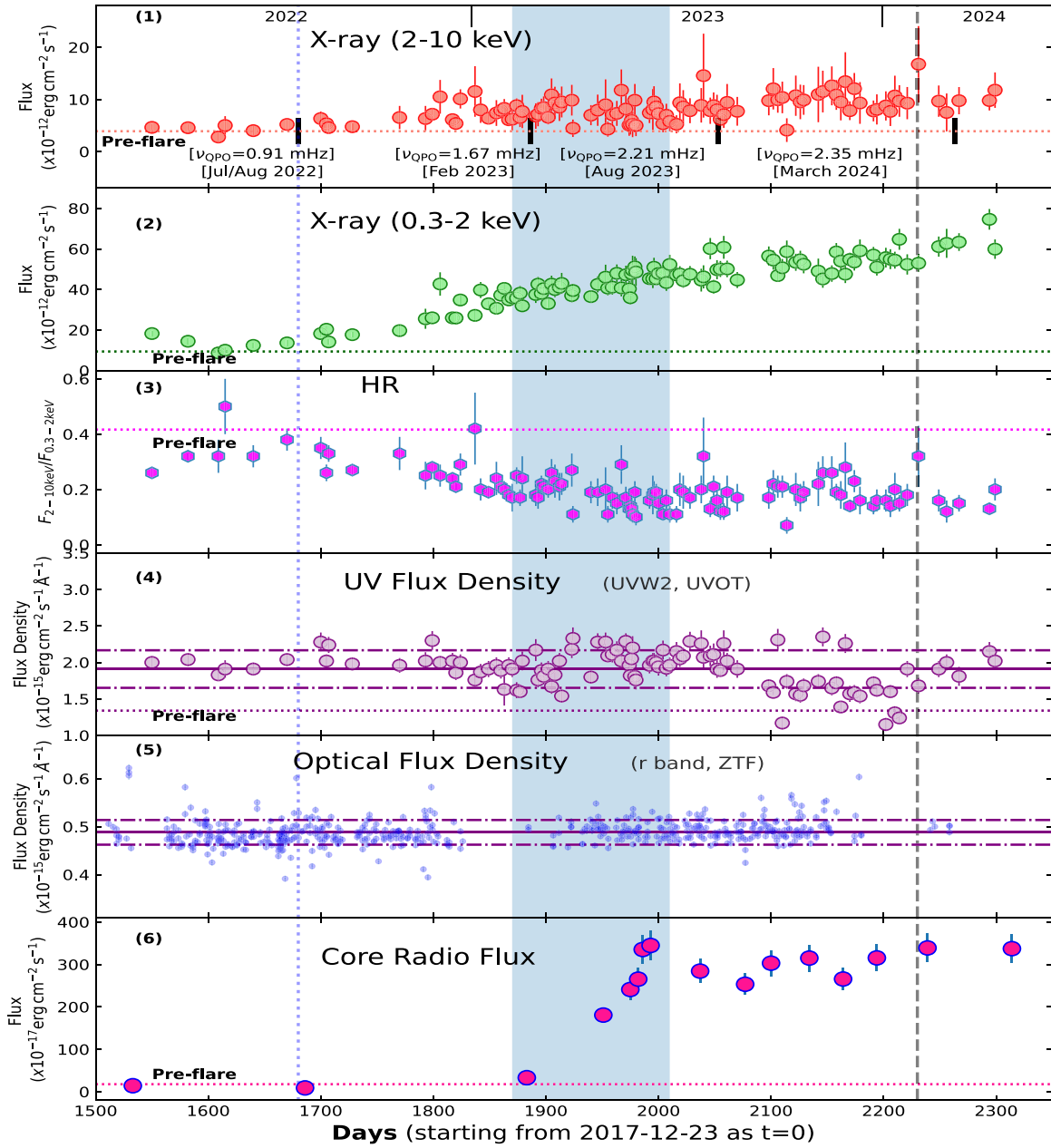


Figure 2. The X-ray, UV, optical, and radio light curves of 1ES 1927+654 during the radio rise, soft X-ray rise, and QPO detection phase (2022 May–2024 April). See Tables 4 and 5 for details. The start date of the light curve is 2017 December 23, corresponding to the burst date reported by B. Trakhtenbrot et al. (2019). The blue shaded region corresponds to the time when we detected the exponential rise in the radio (5 GHz) flux. The radio flux increased by a factor of almost ~ 60 in a matter of a few months. The blue dotted line on the left corresponds to the time (2022 May) when the soft X-ray started to rise, the QPO was detected, and the radio jet was formed. The dashed black line on the right corresponds to the time (2024 February) when we detected spatially resolved jets at 0.1–0.3 pc scales. The dotted horizontal lines in every panel refer to their preflare values (as in 2011 May). From top to bottom, panels show (1) the 2–10 keV X-ray flux (Swift-XRT), (2) the 0.3–2 keV X-ray flux (Swift-XRT), (3) the hardness ratio $F_{2-10 \text{ keV}}/F_{0.3-2 \text{ keV}}$, (4) the UV (UVW2) flux density in units of $10^{-15} \text{ erg cm}^{-2} \text{ s}^{-1} \text{ \AA}^{-1}$ (Swift-UVOT), (5) the optical r -band (ZTF) flux density (in units of $10^{-15} \text{ erg cm}^{-2} \text{ s}^{-1} \text{ \AA}^{-1}$), and (6) the core radio flux at < 1 pc spatial resolution (VLBA, 5 GHz) as reported in E. T. Meyer et al. (2025). The top panel has four vertical lines corresponding to the time when the QPO was detected in the 2–10 keV band using XMM-Newton observations. The QPO frequencies and the date of observations are listed in the top panel. The X-ray flux in units of $10^{-12} \text{ erg cm}^{-2} \text{ s}^{-1}$ is corrected for Galactic absorption.

Table 3). We also note that the soft-excess flux increased by a factor of ~ 10 during this period (see Table 3).

3.2. X-Ray Spectroscopy

As discussed in Section 2.1, we analyzed nine epochs of XMM-Newton EPIC-pn spectra with phenomenological models, and the detailed results are quoted in Table 3. We find that the spectral index steepens from 2011 May, i.e., pre-CL epoch

($\Gamma \simeq 2.44$), to the pre-radio and soft X-ray flare epoch ($\Gamma \simeq 2.6$ –2.8) in 2022 May, reaching $\Gamma \simeq 3.2$ –3.3 during the radio flare. Such steep spectral indices are inconsistent with what is typically observed in Seyfert galaxies (C. Ricci et al. 2017) or quasars (L. Zappacosta et al. 2023). Most of the increase in the soft-excess flux is attributed in this (blackbody) model to the growth of the normalization of the thermal component and not to its temperature. Remarkably, the temperature of the blackbody component remains stable within

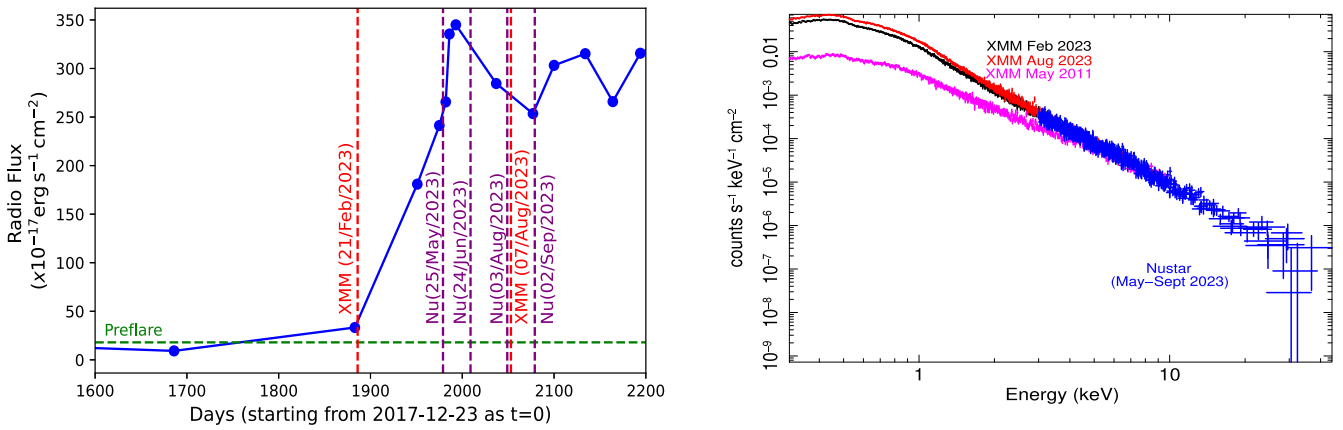


Figure 3. The XMM-Newton and NuSTAR observations of 1ES 1927 coincident with the radio-flaring phase (2023 February–September). Left panel: the radio light curve during the outburst, with the vertical lines denoting the X-ray observations with XMM-Newton (XMM) and NuSTAR (Nu). We note that the radio rise and the plateau phase were well covered by X-ray observations. Right: the three XMM-Newton spectra in the 0.3–10 keV band from the three epochs (preflare: May 2011 in pink; rise of radio: 2023 February in black; high radio: 2023 August in red), along with the NuSTAR spectra in blue from the four epochs during the radio rise (2023 May, June, August, September). We clearly note that the 2–10 keV spectral flux and slope Γ have been nonvariable ($<5\%$) during the radio rise phase. See Tables 3 and 6 for details.

Table 6
X-Ray Spectral Parameters as Obtained from Fitting the NuSTAR Observations, Using the Standard Power-law Model

Models	Parameter(units)	2023 May	2023 June	2023 August	2023 September
Gal. abs.	$N_{\text{H}}(\times)10^{20} \text{ cm}^{-2}$	6.42 (frozen)
Intrinsic. abs.	$N_{\text{H}}(\times)10^{20} \text{ cm}^{-2}$	6.00(frozen)
Power law	Γ	$3.21^{+0.07}_{-0.07}$	$3.21^{+0.07}_{-0.07}$	$3.11^{+0.07}_{-0.07}$	$3.20^{+0.07}_{-0.07}$
	norm(10^{-2})	$1.43^{+0.19}_{-0.17}$	$1.48^{+0.18}_{-0.16}$	$1.23^{+0.15}_{-0.14}$	$1.52^{+0.21}_{-0.18}$
χ^2/dof			519/562		

a rather small range, $kT_{\text{bb}} \sim 0.13\text{--}0.16$ keV. A similar spectral model was applied to the short ($\sim 300\text{--}1500$ s) Swift spectra, yielding very similar results. See Tables 4 and 5.

We do not detect any statistically significant ionized absorption in any of the EPIC-pn spectra. We do not find any trace of an FeK α emission line at ~ 6.4 keV at any of the epochs, consistent with previous studies (C. Ricci et al. 2020, 2021; M. Masterson et al. 2022). The 90% upper limit on the equivalent width of a K α fluorescent line from neutral Fe is $\simeq 120$ eV.

A steep spectrum is confirmed by the four NuSTAR observations taken during the radio flare in 2023 May–September (Table 6). We employed a model constituted by a photoelectrically absorbed power law. The model fits the data well. It confirms a steep spectral index ($\Gamma = 3.1\text{--}3.2$) over the wider energy range of the NuSTAR instruments (i.e., up to $\simeq 30$ keV). If a self-consistent Comptonization model is used (`nthcomp` in XSPEC), the electron temperature is well constrained to $kT_e = 8.4^{+8.8}_{-2.6}$ keV, in a joint simultaneous fit of all four of the NuSTAR observations.

3.3. The Optical and UV Light Curve

The UV flux density of 1ES 1927+654 was monitored using the Swift-UVOT, and we quote the UVW2 band (1928 Å) for consistency with our earlier works. The UV in this time period shows very weak variability, not more than 30% of the mean value (see Table 4 and Figure 2). Thus, the UV variability is not significant. This may indicate a nearly steady rate of accretion. We also plot the optical r -band light curve from ZTF in Figure 2 and find only minimal fluctuations at a timescale of

days. We confirm that there is no optical or UV flaring during this time period.

3.4. Estimating the Total Energy in the 0.3–2 keV Band, the 2–10 keV Band, and the UV Bump

We estimated the total energy pumped into the system during the time interval 2022 May–2024 May by integrating the area under the light curve for the soft (0.3–2 keV) and hard bands (2–10 keV). This was done using the Python `scipy` function `integrate.simps`. The UV energy was estimated by assuming a diskbb of a temperature of $kT = 5$ eV (R. Ghosh et al. 2023), and the normalization was matched at the wavelength 2200 Å with the measured value of the UVW2 filter. We used the mean value of the UVW2 flux density (as in Figure 2) and assumed it to be constant while integrating (as it did not vary beyond 30%). The total integrated energies under the Swift-XRT and UVOT light curves in the 0.3–2 keV, 2–10 keV, and UV bands are 1.56×10^{51} erg, 3.12×10^{50} erg, and 5.76×10^{50} erg, respectively. We clearly find that the total X-ray energy surpasses the energy in the UV, indicating that there may be some other source of energy than that of the UV accretion.

3.5. The Correlations

We used the Python `scipy` function `spearmanr` to estimate the Spearman rank correlation between the hard/soft X-ray and UV fluxes. The Spearman rank coefficient measures the strength of the correlation, and the p -value measures how likely it is that the correlation is not due to chance. For example, a small p -value (typically <0.01) indicates that we

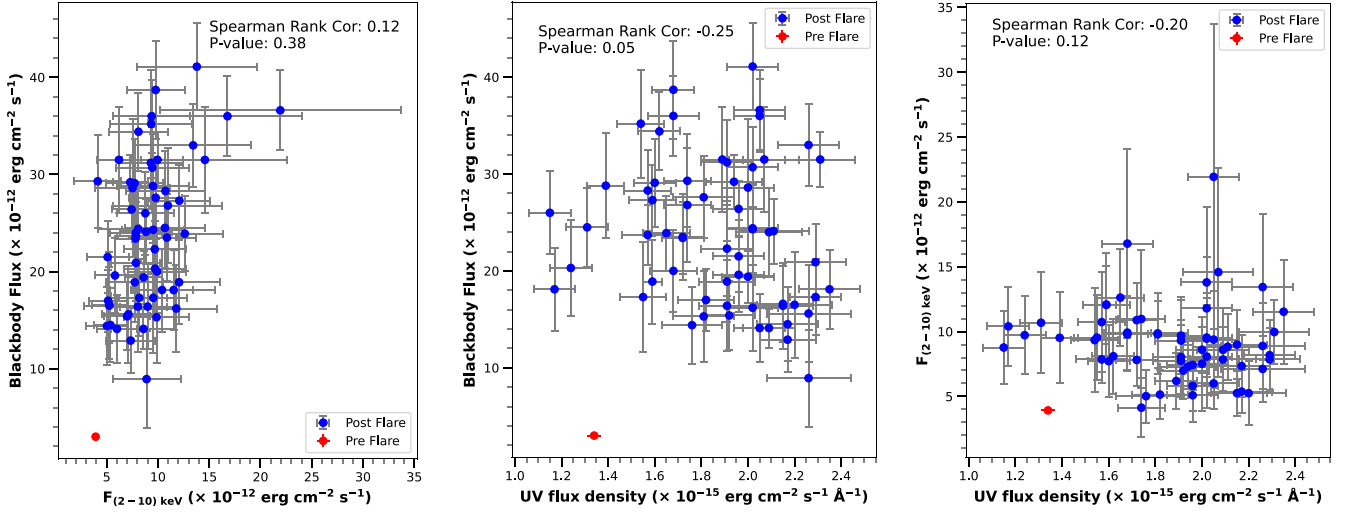


Figure 4. The correlations between the UV flux density, the blackbody flux (soft excess), and the power-law 2–10 keV flux as obtained from Swift observations with a weekly to monthly cadence in the time period 2022 May–2024 April. The red circle denotes the preflare 2011 May observation and is not used in the correlation calculations. Left panel: the blackbody flux vs. the hard X-ray flux (2–10 keV), Middle panel: the blackbody vs. the UV flux density. Right panel: 2–10 keV flux vs. the UV flux density. The Spearman rank correlation coefficient and the p -values are quoted in the panels. None of them show any statistically significant correlation.

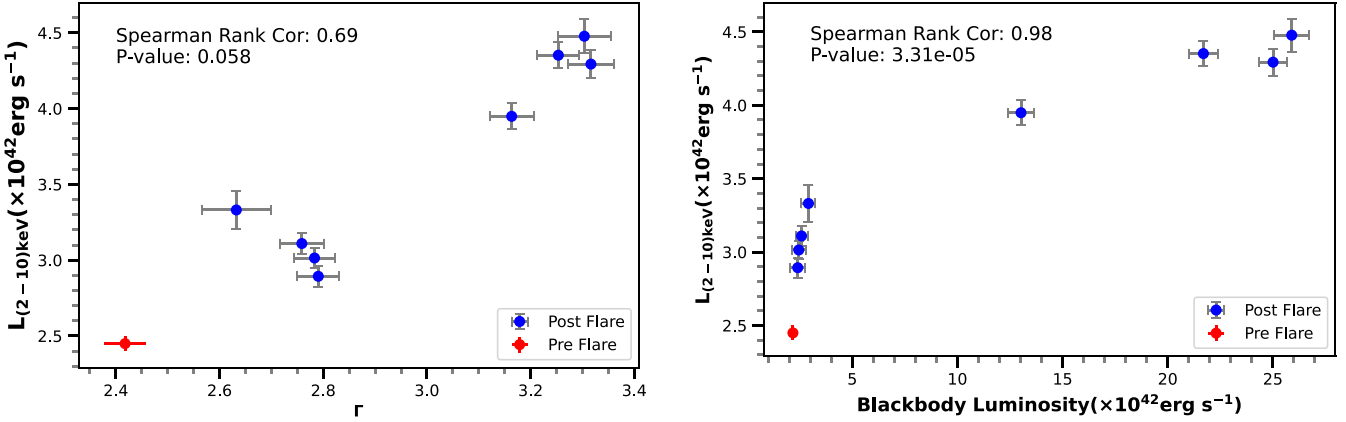


Figure 5. The correlations between the blackbody (soft-excess) luminosity, power-law slope Γ , and power-law 2–10 keV luminosity as obtained from XMM-Newton observations in the time period 2022 July–2024 March. Left: the correlation between the coronal 2–10 keV luminosity and the power-law slope Γ . Right: the correlation between the power-law 2 and 10 keV luminosity and the blackbody luminosity. Table 3 lists the parameters.

can reject the null hypothesis (i.e., no correlation) and conclude that there is a statistically significant relationship between the variables. Figures 4 and 5 show the correlations and their corresponding coefficients and p -values. In Figure 4, involving weekly/biweekly cadence flux values obtained using Swift observations from 2022 May to 2024 April, we do not find any significant correlation between the parameters (UV flux density, soft-excess flux, and the 2–10 keV flux). A Spearman rank correlation test ruled out any correlation at 99.99% confidence.

On the other hand, the observations from XMM-Newton taken sparsely (once in 6 months) over the same time period are ideal to track the longer-term evolution of these quantities. The left panel of Figure 5 shows that there is a strong correlation/trend between the power-law slope and the 2–10 keV luminosity, and the right panel shows a gradual trend of an increase in the 2–10 keV luminosity with the blackbody (soft-excess) luminosity. The red data point in each of the panels denotes the values obtained from the 2011 May XMM-Newton observation when the source was in quiescence (pre-CL) and is not included in the correlation calculations. As a caveat, we

note that in the right panel of Figure 5, although there is a trend of both the soft-excess and power-law luminosity increasing simultaneously, the amount of increase in the 2–10 keV luminosity is smaller (<2 times) compared to the increase in the soft excess (~ 10 times). See Table 3 for details.

4. Discussion

In this paper, we report an episode of large-amplitude (factor of ~ 8) monotonic increase of the soft X-ray 0.3–2 keV in the CL-AGN 1ES 1927+654, over roughly the same timescale as the GHz radio emission increased by a factor of 40–60 as reported in the companion paper by E. T. Meyer et al. (2025). Since 2023 August until 2024 April the core radio emission at 5 GHz has plateaued. However, since 2024 February E. T. Meyer et al. (2025) detected a nascent jet at a 0.1 pc scale, which has progressed to 0.4 pc by 2024 April at a speed of $0.2c$, marking an extraordinary discovery of a jet forming and evolving in real time in a CL-AGN. Our second companion paper, Masterson et al. (2025), detected a mHz QPO in 2022 May ($\nu = 0.93 \pm 0.06$ mHz), which was consistently detected

until March 2024 with an increasing frequency ($\nu = 2.35 \pm 0.05$ mHz as on 2024 March). For the first time in this source a QPO has been consistently detected for ~ 2 yr.

Below we recap the most important observational results from our extensive multiwavelength campaign:

1. The soft excess is still increasing in flux and is now ~ 10 times its pre-CL value (2011 May). The overall soft X-ray (0.3–2 keV) flux is ~ 8 times higher than the pre-CL phase. The best-fit blackbody model temperature (describing the soft excess) is very well constrained in a narrow range 0.13–0.16 keV. We find that the total integrated energy (2022 May–2024 April) under the Swift-XRT and UVOT light curves in the 0.3–2 keV, 2–10 keV, and UV bands are 1.56×10^{51} erg, 3.12×10^{50} erg, and 5.76×10^{50} erg, respectively. The UV accretion energy is clearly lower than the energy pumped into the X-rays.
2. The 2–10 keV power-law slope became softer, $\Gamma = 2.70 \pm 0.04$ in 2022 May to $\Gamma = 3.27 \pm 0.04$ in 2024 March. With NuSTAR 3–40 keV spectra we measured a cutoff temperature of the X-ray corona ($kT_e = 8_{-2}^{+8}$ keV).
3. Coincident with the radio flare in 2023 February–August, the XMM-Newton and NuSTAR observations interestingly show no change in the power-law slope or the 2–10 keV flux ($< 5\%$).
4. We do not detect significant optical or UV flux variability (only $< 30\%$), and only < 2 times variation in the 2–10 keV flux in this epoch of study (2024 May 2022–April).
5. We detect no weeks–month timescale correlation in the variability between the three quantities: UV flux density, soft-excess flux, and 2–10 keV flux. However, in the longer term (~ 2 yr) we detect a trend of increasing spectral slope (Γ) with increasing 2–10 keV flux, as well as an increasing 2–10 keV flux with the soft-excess flux. However, we note that the rise in the 2–10 keV flux is $\lesssim 2$ times.
6. The ratio of the 5 GHz to 2–10 keV flux in this source was $L_{5 \text{ GHz}}/L_{2-10 \text{ keV}} \sim 10^{-5.5}$ in 2022 May, indicating a radio emission dominated by the corona in this radio-quiet source, which is now moving toward the jet-dominated ratio of $\sim 10^{-3}$.
7. We do not detect any FeK α emission line, or any absorption in the 0.3–10 keV spectra.

In light of these observational results, we discuss the following scientific topics in this section. We use a BH mass of $\sim 10^6 M_\odot$ (R. Li et al. 2022), which gives a gravitational radius of $r_g \equiv GM/c^2 = 10^{11}$ cm.

4.1. The Jet-launching Mechanism

Our high-cadence, multiwavelength observations capture the launching of a jet in real time, presenting a unique opportunity to probe jet-launching mechanisms. Here we discuss two prominent jet-launching mechanisms: the Blandford–Znajek (BZ; R. D. Blandford & R. L. Znajek 1977) mechanism, which extracts rotational energy from the BH itself, and the Blandford–Payne (BP; R. D. Blandford & D. G. Payne 1982) mechanism, which extracts rotational energy from the accretion disk. The arguments for/against the BZ and BP models can be

summarized into four categories: (i) outflow collimation, (ii) outflow speed, (iii) outflow trigger, and (iv) outflow efficiency.

4.1.1. Outflow Collimation

The collimation of the 1ES 1927 outflow suggests a BZ “jet” origin rather than a BP disk “wind” origin. A disk wind generally has a wide, nearly isotropic opening angle, compared to a much narrower, more collimated relativistic jet. Therefore, the spatially resolved, bilobed structure of the radio emission reported by E. T. Meyer et al. (2025) supports the BZ mechanism over the BP mechanism.

4.1.2. Outflow Speed

Radio measurements suggest a mildly relativistic outflow speed of $0.2c$ (E. T. Meyer et al. 2025). BP winds can have speeds of $0.2c$ only if they are launched from quite close ($\lesssim 10r_g$) to the BH (R. D. Blandford & D. G. Payne 1982), while a speed of $0.2c$ is somewhat low for the BZ mechanism (R. D. Blandford & R. L. Znajek 1977). However, this low speed could be an inclination angle effect. If the jet contains a faster-moving jet spine that is Doppler beamed away from the line of sight, the observations may only measure the slower-moving jet sheath. Future observations of the jet’s evolution will better constrain its speed and therefore help discriminate between jet-launching mechanisms.

4.1.3. Outflow Trigger

The proposed trigger for the outflow is a reconfiguration of the magnetic field close to the BH. The magnetic energy density close to the BH likely remains relatively constant since the hard X-ray flux, powered by reconnection/turbulence in the corona, increases by less than a factor of two over the observational period. The flux needed to change the dominant magnetic components close to the BH could have accumulated since the previous 1ES 1927 CL event associated with an inversion of the magnetic field polarity in a magnetically dominated accretion disk (N. Scephi et al. 2021; S. Laha et al. 2022). Since that CL event, accretion through a canonical thin disk (N. I. Shakura & R. A. Sunyaev 1973) onto the BH proceeds normally, as inferred from the relatively constant UV flux (Figure 2, fourth panel). As accretion occurs, magnetic flux can advect onto the BH over the viscous timescale t_{visc} :

$$t_{\text{visc}} = 18 \left(\frac{r}{100r_g} \right)^{3/2} \left(\frac{M}{10^6 M_\odot} \right) \alpha_{0.1}^{-1} h_{0.1}^{-2} \text{ months}, \quad (1)$$

where r is the radial distance from the BH, M is the BH mass, $\alpha_{0.1}$ is the viscosity parameter in units of 0.1, and $h_{0.1}$ is the disk aspect ratio H/r in units of 0.1. For these estimated upper limit parameters, the 18-month interval between the CL event and the start of the radio flare would imply that the magnetic flux was advected from a spatial scale of $100r_g$. This spatial scale decreases for smaller values of α and h . However, it will increase if the inner region is a thick flow rather than a thin disk (J. Dexter & M. C. Begelman 2019).

If poloidal magnetic flux is advected toward the event horizon from the inner accretion disk, it could trigger either the BZ mechanism or the BP mechanism since both rely on the configuration of the magnetic field (R. D. Blandford & R. L. Znajek 1977; R. D. Blandford & D. G. Payne 1982).

In principle, this advection could occur without changing the accretion rate and therefore maintain a relatively constant UV flux. However, a BP wind would likely remove angular momentum from the disk (R. D. Blandford & D. G. Payne 1982), thereby lowering the accretion rate and decreasing the UV flux from the accretion disk. Therefore, the nearly steady UV flux suggests that the jet launch occurs owing to the BZ mechanism.

4.1.4. Outflow Efficiency

The radio power of the 1ES 1927 outflow implies a high efficiency. The power expected for a BZ jet from a rapidly spinning (i.e., maximally efficient) BH with spin parameter $a \approx 1$ is

$$P_{\text{BZ}} \approx \frac{\kappa\pi c}{4} r_g^2 B^2 \text{ erg s}^{-1}, \quad (2)$$

where $\kappa \simeq 0.05$ (A. Tchekhovskoy et al. 2011) and B is the net vertical magnetic flux accumulated on the BH horizon, i.e., at length scales of a few $r_g \sim 10^{-7}$ pc.

The magnetic field close to the BH is likely well above equipartition values, due to the nature of the corona. The corona comprises electrons with temperatures $\sim 10^9$ K that sit a distance $R_c \lesssim 10r_g$ from the BH (X-ray variability and microlensing constraints; A. C. Fabian et al. 2009; X. Dai et al. 2010; E. Kara et al. 2013; D. R. Wilkins et al. 2021; S. Laha et al. 2024). These electrons inverse Compton scatter disk photons to produce hard X-rays (e.g., J. I. Katz 1976; L. A. Pozdnyakov et al. 1977). To maintain these high electron temperatures, the corona must be magnetically dominated (A. Merloni & A. C. Fabian 2001). Assuming that some fraction of the magnetic energy in the X-ray corona converts into hard X-rays yields a minimum coronal magnetic field strength of

$$B_0 \geq 10^4 \text{ G} \left(\frac{L_{2-10}}{10^{43} \text{ erg s}^{-1}} \right)^{1/2} \left(\frac{R_c}{10r_g} \right)^{-1} \left(\frac{M}{10^6 M_\odot} \right)^{-1}, \quad (3)$$

where the 1ES 1927 luminosity $L_{2-10} \sim 10^{43}$ erg s⁻¹ (Table 3). Recent analytic calculations and particle-in-cell simulations of the dissipative and radiative processes in the coronal plasma yield magnetic fields of up to $B_0 \sim 10^8 \text{ G} (M/10 M_\odot)^{-1/2} = 3 \times 10^5 \text{ G}$ (e.g., A. M. Beloborodov 2017; D. Grošelj et al. 2024). Large B_0 values on event horizon scales are feasible considering that measurements from AGN jets have previously found magnetic field strengths of ~ 0.1 G on ~ 1 pc scales from core frequency-shift methods (S. P. O’Sullivan & D. C. Gabuzda 2009) and ~ 10 G on ~ 0.1 pc scales from Faraday rotation measurements (I. Martí-Vidal et al. 2015). Recent VLBI measurements have also suggested kilogauss fields close to the BH (M. Lisakov et al. 2025). Such observational values are consistent with $B_0 \gtrsim 10^5$ G at the base of the jet with a $1/r$ decay of the magnetic field and are thereby consistent with theoretical and numerical predictions for launching relativistic jets (R. D. Blandford & R. L. Znajek 1977; A. Tchekhovskoy et al. 2011).

Plugging this value for the magnetic field into Equation (2), the BZ power is $P_{\text{BZ}} \approx 3 \times 10^{42}$ erg s⁻¹. This power is on the order of the jet kinetic power estimated from the elevated radio state of 1ES 1927+654 (E. T. Meyer et al. 2025). The high jet kinetic power implies that the BZ jet must convert into

radiation at close to 100% efficiency. Because the BZ mechanism is more efficient than the BP mechanism, this high efficiency suggests that the jet launches via the BZ mechanism.

4.2. Characteristics of the Radio Emission

4.2.1. The Radio Emission as Optically Thin Synchrotron Emission

The observed radio spectral slopes between 5–8.4 GHz and 8.4–23.6 GHz indicate a nature consistent with a small-scale synchrotron jet/outflow (E. T. Meyer et al. 2025). The spectrum is curved and peaks around 5 GHz, and it resembles the typical profile of GHz-peaked spectrum AGN sources. The relatively steep late-time spectral index (α where $F_\nu \sim \nu^{-\alpha}$) between 8.4 and 23.6 GHz ($\alpha = 1.05 \pm 0.26$) suggests that the emission is dominated by synchrotron processes from an optically thin region, aligning with the characteristics expected from jet emissions. For the expected magnetic field of ~ 0.2 G at 0.1 pc, an electron with Lorentz factor $\gamma = 100$ emits synchrotron emission at 5 GHz. Such an electron would lose half its energy owing to synchrotron emission after traveling for about a parsec, i.e., at 0.1 pc it has not lost much energy as a result of synchrotron cooling (the slow cooling regime). In the slow cooling regime, the spectral index α relates to the underlying electron distribution’s power-law index p as $p = 2\alpha + 1$ rather than $p = 2\alpha - 1$ as in the fast cooling regime (G. R. Blumenthal & R. J. Gould 1970). Therefore, the measured 5–8 GHz emission’s $\alpha \sim 0.5$ (E. T. Meyer et al. 2025) gives an electron power-law index of $p \sim 2$, which is a reasonable value from magnetic reconnection. The increase in the 8–22 GHz band to $\alpha \sim 1$ suggests the presence of a cooling break in that frequency range, indicating that the electrons now emit most of their energy as synchrotron radiation.

4.2.2. The 200-day Delay of the Radio Flare from the Start of the Soft X-Ray Rise

The delay in the radio increase of ~ 200 days relative to the soft X-ray rise could be due to obscuration by an external screen of hot gas that blocks the expected emission via free-free absorption until the jet emerges from behind it (see Figure 6). If this external screen sits at the estimated distance of the broad-line region (BLR), approximately 30–40 lt-day ($\sim 10^{17}$ cm; B. Trakhtenbrot et al. 2019), the screen will absorb all synchrotron emission until the jet propagates past it, i.e., after ~ 200 days for a jet speed of $0.2c$ (E. T. Meyer et al. 2025). The frequency where an ionized gas at a temperature of 10^4 K becomes optically thin to free-free absorption is proportional to $nL^{1/2}$, where n is the number density of the gas and L is the path length through the absorbing gas. The necessary combination of number density and path length could come from a localized overdensity from, e.g., gas that was expelled during the previous CL event or compressed owing to radiation pressure (A. Baskin & A. Laor 2021). We note that the length of the delay requires that the free-free absorption comes from an external screen rather than from hot gas spatially colocated with the jet. The higher-frequency X band ~ 8 GHz became optically thin before the lower frequency ~ 5 GHz during the radio flare (E. T. Meyer et al. 2025), which is consistent with the optical depth from free-free absorption $\tau \sim \nu^{-2}$, though not exclusive to it. Figure 6 shows the formation and evolution of jet, along with the soft X-ray rise in this source. The effect of the external screen is also depicted in the cartoon. In addition, if the radio emission were from

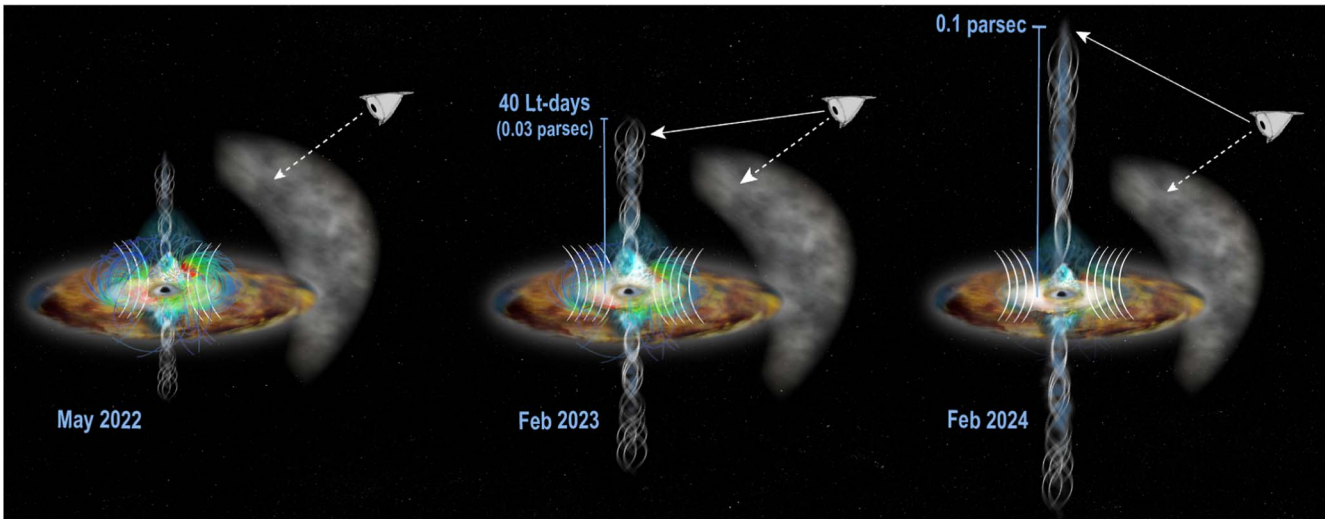


Figure 6. Cartoon depicting the spectacular accretion disk, corona, and jet evolution in the enigmatic CL-AGN IES 1927+654. Panels from left to right give us the temporal evolution of the system, which includes the soft X-ray rise, QPO detection, jet formation, and jet evolution. Left panel (2022 May): this is the time when the soft X-ray started to rise and the jet and the QPO (~ 0.91 mHz) were formed. The accretion disk is shown in brown, the random magnetic field is denoted by colored lines (red and cyan), and the advected poloidal fields (responsible for jet formation) are shown in white. The tenuous white cloud corresponds to the external screen of hot gas that blocks the expected radio emission via free-free absorption. This hot screening gas may possibly be the BLR clouds located at ~ 30 – 40 lt-day (as detected by B. Trakhtenbrot et al. 2019). The eye denotes the observer, and the dotted lines denote the line of sight to the central engine, while the solid lines denote a view toward the jet. We note that although the jet may be formed at the same time as the soft X-ray rise and the QPO, we could not detect it because of the free-free absorption of the screening gas. Middle panel (2023 February): same as the left panel, but the jet has now evolved beyond 30 – 40 lt-day (0.03 pc) and hence has come out of the BLR screen, which is visible as the radio flare continuing for a few months (2023 February–August). The radio emission gets plateaued once the jet has fully come out (sometime in 2023 August). The soft X-rays from the inner disk (white patch in the disk) have gained in strength compared to those in 2022 May. Variability in the XMM-Newton soft X-ray light curve on the order of 200 – 300 s constrains the soft X-ray emission to originate from within $\sim 100r_g$ of the BH. Right panel (2024 February): same as the middle panel, but the jet has now evolved beyond 0.1 pc, which corresponds to the spatial resolution of VLBA, and hence we can detect spatially resolved bipolar jets. The soft X-rays are now extremely bright (by a factor of ~ 8) compared to those in 2022 May. In all the panels note that the UV disk (denoted in brown) has a nearly steady rate of accretion, as does the corona (the cyan triangular shape at the center), which does not show much variability in flux. See Tables 3 and 6 and Figure 2 for reference.

synchrotron self-absorbed electrons only on smaller scales, say, $\sim 1000r_g$, the radio rise should occur after a propagation time of only ≈ 2 days for the measured jet velocity of $0.2c$. Hence, the delay must be due to an external screen.

4.3. The Nature of the Soft Excess

The origin of the soft excess in radio-quiet (RQ) AGN is highly debated (see, e.g., J. Crummy et al. 2006; B. Vaia et al. 2024). In IES 1927+654 the evolution/rise of the soft excess (modeled by blackbody) coincided with the formation and evolution of the radio jet, along with the softening of the power-law emission and the appearance of a QPO. Overall, we note the following: (1) the soft-excess light curve monotonically increased by a factor of ~ 10 (Table 3); (2) the temperature of the blackbody is very narrowly constrained in the range 0.14 – 0.16 keV during the entire rise phase (see Tables 3, 4, and 5), and there is no correlation between the soft-excess flux and the temperature; and (3) the soft X-ray, hard X-ray, and UV fluxes do not correlate with each other, indicating that they arise from physically distinct regions. This new soft excess can be explained neither with (i) the hard X-ray disk-reflection model (J. Garcia et al. 2014), because we observe no substantial variation in the 2 – 10 keV flux, nor with (ii) the “warm Comptonization” scenario (C. Done et al. 2012), because we do not observe any increase in the UV flux in a similar time span.⁴¹ All these point to the fact that the origin of the new soft excess in IES 1927+654 is unique and not the one

we find in RQ-AGN. The origin of the soft excess can possibly be related to the available magnetic energy and the jet emission.

The total integrated energies under the Swift-XRT and UVOT light curves in the 0.3 – 2 keV, 2 – 10 keV, and UV bands are 1.56×10^{51} erg, 3.12×10^{50} erg, and 5.76×10^{50} erg, respectively. The total X-ray energy surpasses that of the UV, indicating that a source of energy extraction other than that of the standard accretion disk (UV) is at play. This is also demonstrated in Figure 7, where the soft X-rays show a larger energy dissipation compared to the hard X-rays. Additionally, the total jet power and soft-excess luminosity are comparable ($\sim 10^{43}$ erg s^{-1}), suggesting that the rise of soft X-rays could be magnetically powered, for example, through a change in the magnetic field topology or the presence of the jet. For example, the increase in soft X-rays after the jet launches could be related to a change in magnetic field structure in the innermost disk, or a change in the emitting volume caused by the presence of the jet. Variability in the XMM-Newton soft X-ray light curve on the order of 200 – 300 s constrains the soft X-ray emission to originate from within $\sim 100r_g$ of the BH. Detailed spectral and timing analysis of the soft X-ray spectra will be carried out in a future work.

4.4. The Unusual Coronal Emission and the Disk–Corona–Jet Relation

The 2 – 10 keV coronal emission in the source IES 1927+654 has been unusual since the CL event. In Figure A1 in the Appendix we show the entire multiwavelength light curve of this source from the previous CL phenomenon (2017

⁴¹ This model could, however, be applicable if the assumption that the energy source for the soft excess is the standard disk accretion (in UV) is relaxed.

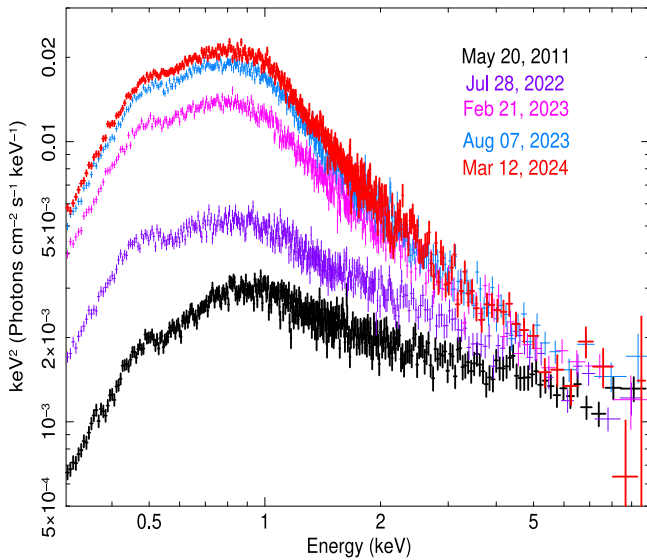


Figure 7. The overplotted EPIC-pn spectra of 1ES 1927+654 showing the evolution of the total energy dissipated per keV across the 0.3–10 keV band. The different colors denote the different dates of observation. The topmost spectrum (in red) with the highest energy in the soft X-rays denotes the latest observation in 2024 March. In comparison, the preflare (or pre-CL) phase in 2011 May in black shows much less energy in the soft X-ray band. We note here that the 2–10 keV band does not show radical changes for different epochs, compared to the soft X-rays. We have only included observations from 2022 July to 2024 March to cover the soft X-ray rise, and we have plotted the 2011 May observation for comparison. See Table 3 for details. The figure has been created using the `setplot area` and `plot uuef` commands in XSPEC.

December) until 2024 April. This is perhaps the only source where the corona completely vanished and reappeared in a month timescale during the CL event (C. Ricci et al. 2020, 2021; S. Laha et al. 2022). The pre-CL power-law slope ($\Gamma = 2.45$) has been on the higher end of AGN Γ distribution (A. Tortosa et al. 2018). During the violent CL event just prior to the vanishing of the corona in 2018 August, we detected a very soft power-law slope $\Gamma \sim 4\text{--}5$ (C. Ricci et al. 2020, 2021; S. Laha et al. 2022; C. Ricci & B. Trakhtenbrot 2023), very unusual for an AGN, along with an abnormally low electron temperature ($kT_e \sim 1.5$ keV). As the X-ray corona was destroyed and then re-created, the spectral slope was again very soft with $\Gamma \sim 3$ (C. Ricci et al. 2020).

Very recently in 2022 May, after the soft X-ray started to rise along with the advent of a QPO and a radio jet, we noticed that the coronal slope again gradually became softer (over a period of ~ 1 yr), from $\Gamma = 2.79$ in 2022 August to $\Gamma = 3.32$ in 2024 March. With broadband NuSTAR observations in 2023 May–September coinciding with the exponential radio rise, we measured a constant coronal slope of $\Gamma \sim 3.2$ and an electron temperature of $kT_e = 8.4^{+8.8}_{-2.6}$ keV (with the thermal Comptonization model `nthcomp` in XSPEC). The corona is cooler than the typical ones found in normal AGN. Interestingly, low coronal temperatures have been observed in super-Eddington systems (A. Tortosa et al. 2023) and predicted theoretically from general relativistic magnetohydrodynamic simulations (F. Pacucci & R. Narayan 2024) and analytical calculations (P. Madau & F. Haardt 2024). However, 1ES 1927+654 is still sub-Eddington as obtained in Section 2.2.1 ($\lambda_{\text{Edd}} \approx 0.3$), and hence it is unusual.

There exists a strong correlation between the 5 GHz and 2–10 keV flux in RQ-AGN, which is also found in coronally

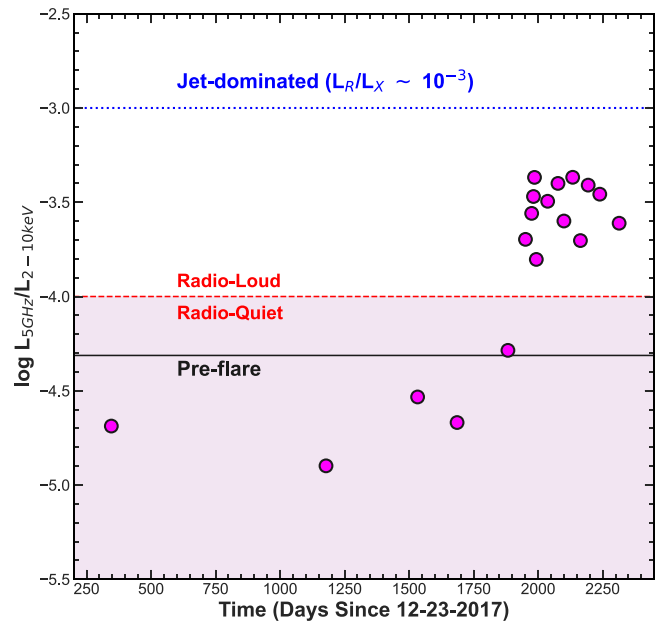


Figure 8. 1ES 1927+654 jumping out of the radio-quiet regime. The ratio between 5 GHz radio peak luminosities and 2–10 keV X-ray luminosities (aka radio-loudness parameter) is plotted as a function of days since the flare on 2017 December 23. The black solid line represents the preflare ratio, with semicontemporaneous radio and X-ray fluxes taken from S. Laha et al. (2022). The blue dotted line marks the boundary between radio-loud (RL) and radio-quiet (RQ) AGN as introduced by F. Panessa et al. (2007), distinguishing Seyfert galaxies from low-luminosity radio galaxies of $L_R/L_X \approx 10^{-3}$. The red dashed line denotes the classical division between RL-AGN and RQ-AGN by Y. Terashima & A. S. Wilson (2003). The filled colored area indicates the phase space ($10^{-6} < L_R/L_X < 10^{-4}$) encompassed by coronal emission from radio-quiet AGN, based on the well-established relation for coronally active cool stars of $L_R/L_X = 10^{-5}$ (M. Gdel & A. O. Benz 1993; A. Laor & E. Behar 2008).

active stars (M. Gdel & A. O. Benz 1993; A. Laor & E. Behar 2008), known as the Gdel–Benz (GB) relation, with a typical value of $10^{-5.5}$. During the violent CL event in 2018–2019 until the end of 2022, the ratio of radio to X-ray flux of 1ES 1927+654 was within the GB range (S. Laha et al. 2022; R. Ghosh et al. 2023), indicating that the bulk of radio emission was from the corona. The 5 GHz core (< 1 pc scale) radio emission was lowest during the coronal destruction in 2018, indicating again that the low level of radio emission (~ 2 mJy) had a coronal origin. Since early 2023, when the radio flux started to rise, the ratio has assumed higher values, mostly because there is no associated increase in the 2–10 keV flux. We note that the hard X-ray 3–40 keV flux and its slope, as determined from four NuSTAR observations coinciding with the radio exponential rise, remain unchanged at the $< 5\%$ level (Figure 3 and Table 6). This indicates that the excess radio emission is coming from something other than the corona, possibly a jet. In Figure 8, we have plotted the evolution of the GB ratio of the source during the radio flare, and we note that the initially radio-quiet source is now moving toward the jet-dominated ratio of $\sim 10^{-3}$ (F. Panessa et al. 2007).

4.5. The QPO–Jet Relation

The rise of the soft X-ray flux in 2022 coincides with the emergence of a QPO feature in the X-rays (M. Masterson et al. 2025), which could be when the jet is formed as well. The QPO is more strongly detected in the hard X-ray band (above 2 keV), with much less significance in the soft X-ray band, possibly

indicating that the QPO is primarily associated with the “corona” of the AGN. Very few SMBHs have shown QPOs to date, such as RE J1034+396 (M. Gierliński et al. 2008) and ASASSN-14li (D. R. Pasham et al. 2019). To date, no SMBH QPO shows the dramatic frequency evolution that is seen in the QPO in 1ES 1927+654 (see Masterson et al. 2025 for further comparisons with existing SMBH QPOs).

Observations have indicated that in BH binaries (BHBs) the advent of QPOs is sometimes also associated with a radio outburst and a subsequent ejection of a radio jet. Type B QPOs are closely related to the production of jetlike outflows (S. Corbel et al. 2001; E. Gallo et al. 2004; J. C. A. Miller-Jones et al. 2012; T. D. Russell et al. 2019), but a physical model is yet to be developed. As a BHB transitions from the hard to a soft state, a strong (type C) low-frequency QPO appears in the power spectral density (R. A. Remillard et al. 2002; P. Casella et al. 2005). Their frequencies increase from ~ 0.01 to 10 Hz as the spectrum softens. After some time during this transition, the type C QPOs and the associated strong band-limited red noise are replaced by a type B QPO (~ 4 –9 Hz) with a considerably weaker band-limited noise (P. Casella et al. 2005; T. M. Belloni 2010; A. R. Ingram & S. E. Motta 2019; J. Homan et al. 2020), which is then associated with a radio outburst and a jet. This has never been observed in an AGN. The new QPO in 1ES 1927 is remarkable, in that (1) it is consistently found for ~ 2 yr, (2) its frequency increases with time, (3) the QPO is most prevalent in the hard X-rays, and (4) its frequency ($\nu = 1$ –2 mHz) does not seem to line up with a BHB analogy, because a simple linear scaling of the frequency with mass to a type B QPO would require the BH mass of 1ES 1927+654 to be $< 5 \times 10^4 M_{\odot}$. The time evolution of its frequency (increase in frequency with time) also does not follow the BHB pattern. However, the nearly simultaneous occurrence of the QPO and the jet in 1ES 1927+654 points to physics very closely related to the ones in BHB, and this is an important discovery in the field of AGN. For example, the increase of the frequency indicates that the physical size of the QPO-emitting region is shrinking with time. This is in agreement with the evolution of the X-ray spectral index, indicating more intense Compton cooling as expected in a more compact corona. Similar behavior is routinely seen in X-ray binaries, whereby all characteristic frequencies increase as the spectrum softens (T. M. Belloni 2010). This is often interpreted in the context of the truncated disk model (C. Done et al. 2007), whereby the disk inner radius and therefore the size of the corona reduce as the spectrum softens. Reflection spectroscopy reveals that the disk inner radius does indeed reduce as the luminosity increases, even though there is widespread disagreement over the precise location of the disk inner radius (see, e.g., J. A. Garcia et al. 2015). Suggested physical mechanisms for a moving truncation radius include evaporation/condensation (D. M. Eardley et al. 1975; M. Mayer & J. E. Pringle 2007) and magnetic truncation (M. T. P. Liska et al. 2022). Our companion work (Masterson et al. 2025) explores a variety of explanations for the QPO in 1ES 1927+654, and we refer the reader to that paper for further details. A future work will carry out a detailed theoretical study connecting the jet and the QPO of this source and will also explore other possible models/interpretations.

5. Conclusions

In this paper, we report an episode of large-amplitude (factor of ~ 8) monotonic increase of the soft X-ray 0.3–2 keV in the CL-AGN 1ES 1927+654, over roughly the same timescale as the

GHz radio emission increased by a factor of 40–60 as reported in the companion paper by E. T. Meyer et al. (2025). In addition, E. T. Meyer et al. (2025) detected a spatially resolved radio jet evolving at a speed of $\sim 0.2c$ in a scale of 0.1–0.3 pc, and Masterson et al. (2025) detected a consistent QPO in the hard X-rays with increasing frequency, both of which are extraordinary and rare events in an AGN. We list below the most important conclusions from this extensive multiwavelength study.

1. Jet emission mechanism: The weak variation of the 2–10 keV X-ray emission and the nearly steady UV emission suggest that the magnetic energy density and accretion rate are relatively unchanged and that the jet could be launched owing to a reconfiguration of the magnetic field (toroidal to poloidal) close to the BH. Advecting poloidal flux onto the event horizon would trigger the BZ mechanism, leading to the onset of the jet. The concurrent softening of the coronal slope (from $\Gamma = 2.70 \pm 0.04$ to $\Gamma = 3.27 \pm 0.04$), occurrence of a QPO, and low coronal temperature ($kT_e = 8_{-3}^{+8}$ keV) during the radio outburst suggest that the poloidal field reconfiguration can significantly impact coronal properties and thus influence jet dynamics. These extraordinary findings in real time are crucial for coronal and jet plasma studies, particularly as our results are independent of coronal geometry.
2. The absorbing screen and late-time jet evolution: The 200-day delay of the radio flare from the start of the soft X-ray rise could be due to a screen of hot gas that blocks the expected emission via free-free absorption until the jet emerges from behind it. If this external screen sits at the estimated distance of the BLR, approximately 30–40 lt-day ($\sim 10^{17}$ cm B. Trakhtenbrot et al. 2019), the screen will absorb all synchrotron emission until the jet propagates past it, i.e., after ~ 200 days for a jet speed of $0.2c$. See Figure 6.
3. The origin of the soft excess: We note that (1) the soft-excess light curve monotonically increased by a factor of ~ 10 , (2) the temperature of the blackbody (modeling the soft excess) is very narrowly constrained in 0.14–0.16 keV (see Figure A2) during the entire rise phase, (3) variability in the XMM-Newton soft X-ray light curve on the order of 200–300 s constrains the soft X-ray emission to originate from within $\sim 100 r_g$ of the BH, and (4) there is no correlation of the soft-excess flux with the hard X-ray and UV fluxes. The total integrated energies under the Swift-XRT and UVOT light curves in the 0.3–2 keV, 2–10 keV, and UV bands are 1.56×10^{51} erg, 3.12×10^{50} erg, and 5.76×10^{50} erg, respectively. The energetics of the UV accretion therefore cannot account for the jet and the soft X-ray rise, implying an additional source of energy in action. A gradual rise in the soft excess by a factor of ~ 10 times in 2 yr, along with the radio flare and their mutually similar luminosity $L_{\text{soft excess}} \sim L_{\text{radio jet}} \sim 10^{43} \text{ erg s}^{-1}$, points toward a related origin, which could be powered by the magnetic fields in the inner regions of the accretion disk.
4. The jet–QPO relation: the occurrence of a QPO nearly simultaneously with the jet signals some interesting similarity with BHBs, where observations have detected QPO and jets to occur simultaneously. However, there is no direct analog of the QPO frequency and its evolution as detected in 1ES 1927+654 with the BHB systems. As

the QPO frequency increased over a time period of 2 yr, we detected a steeper photon index ($\Gamma \sim 3.3$) and a cool corona ($kT_e = 8.4_{-2.6}^{+8.8}$ keV), accompanied by the formation and evolution of the jet. We refer to Masterson et al. (2025) for several other interpretations of the QPO origin.

5. The jet–corona relation: we do not find any connection between the radio and the 2–10 keV (coronal) flux variations over the period of 2 yr (2022 May–2024 April). The 2–10 keV flux varied only by a factor <2 , with a softening power-law slope ($\Gamma = 2.7\text{--}3.2$), while the radio emission flared by a factor of ~ 60 and plateaued at a high flux state. In particular, we do not detect any change ($<5\%$) in coronal flux and power-law slope Γ during the exponential radio flare (2023 February–August). The ratio of the 5 GHz to 2–10 keV flux in this source was $L_{5\text{ GHz}}/L_{2\text{--}10\text{ keV}} \sim 10^{-5.5}$ in 2022 May, indicating a radio emission dominated by the corona in this radio-quiet source, which is now moving toward the jet-dominated ratio of $\sim 10^{-3}$ (see Figure 8).

Acknowledgments

The material is based on work supported by NASA under award No. 80GSFC21M0002. J.S. acknowledges the Czech Science Foundation project No. 22-22643S. S.L. is grateful to

Jay Friedlander, who has created the graphics of the jet and the heated gas (Figure 6). C.R. acknowledges support from Fondecyt Regular grant 1230345 and ANID BASAL project FB210003. F.R. and S.B. acknowledge funding from PRIN MUR 2022 SEAWIND 2022Y2T94C, supported by European Union–Next Generation EU. S.B. acknowledges support from INAF LG 2023 BLOSSOM. M.P. acknowledges the support of the Inter-University Centre for Astronomy and Astrophysics (IUCAA), Pune through the Visiting Associate Programme. M.N. is supported by the European Research Council (ERC) under the European Union’s Horizon 2020 research and innovation program (grant agreement No. 948381) and by UK Space Agency grant No. ST/Y000692/1. S.L., E.M., and E.B. acknowledge support from NSF-BSF grant Nos. NSF-2407801 and BSF-2023752.

Appendix

The long term multiwavelength light curve of the source is shown in Figure A1, which includes the previous changing-look phase as well as the recent QPO+jet phase.

Figure A2 shows the correlations between the soft X-ray excess blackbody temperature (kT) and other physical parameters. We find no correlation, and most importantly, the temperature is very narrowly constrained between 0.14–0.16 keV during the entire QPO+jet phase.

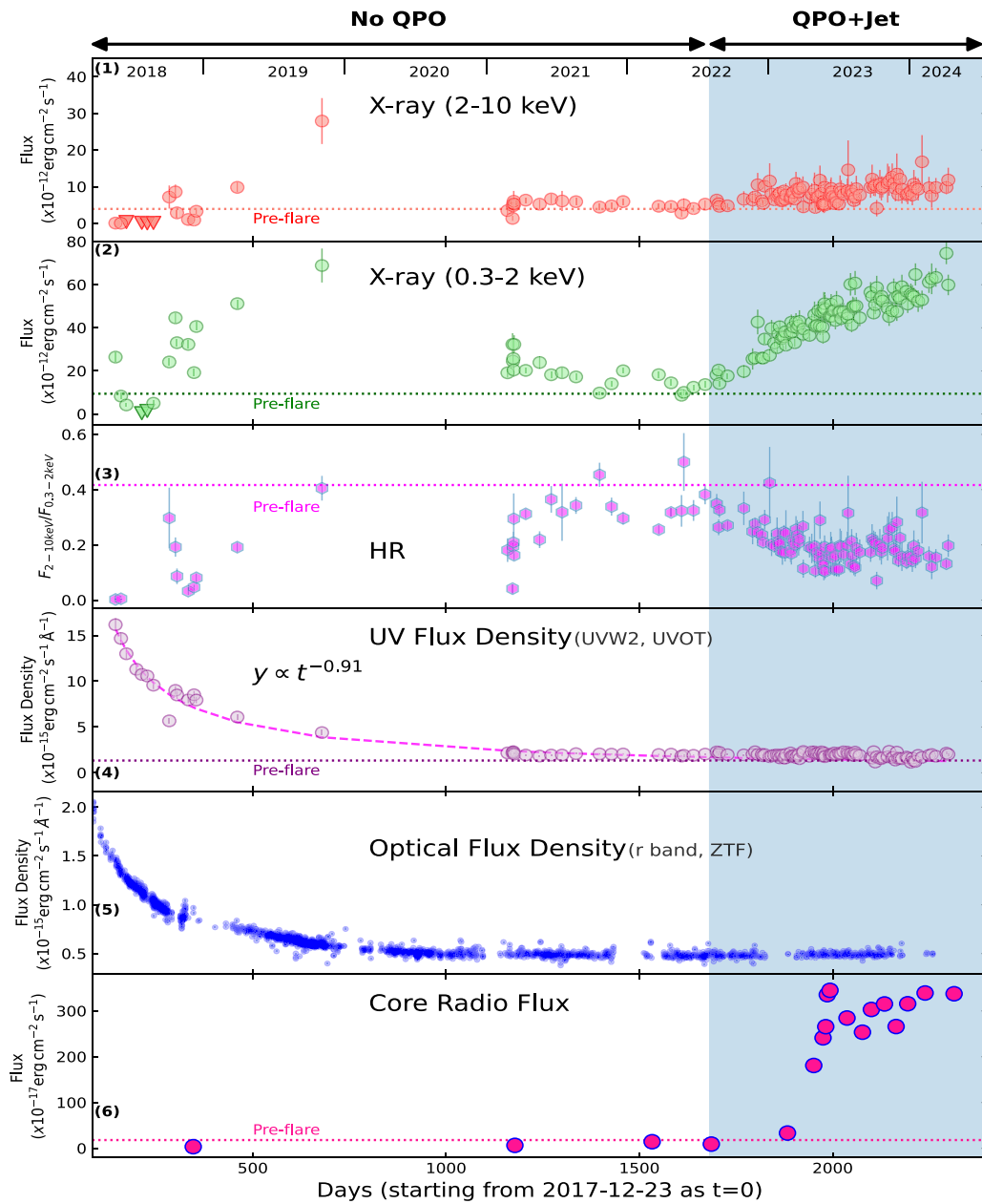


Figure A1. The X-ray, UV, optical, and radio light curves of 1ES 1927+654 during the period from 2018 May (when the first CL outburst happened and Swift monitoring started) to 2024 April. The recent QPO+jet+soft X-ray rise phase is shaded in blue. See Table 4 and S. Laha et al. (2022) and R. Ghosh et al. (2023) for details. The different panels are the same as the ones discussed in Figure 2.

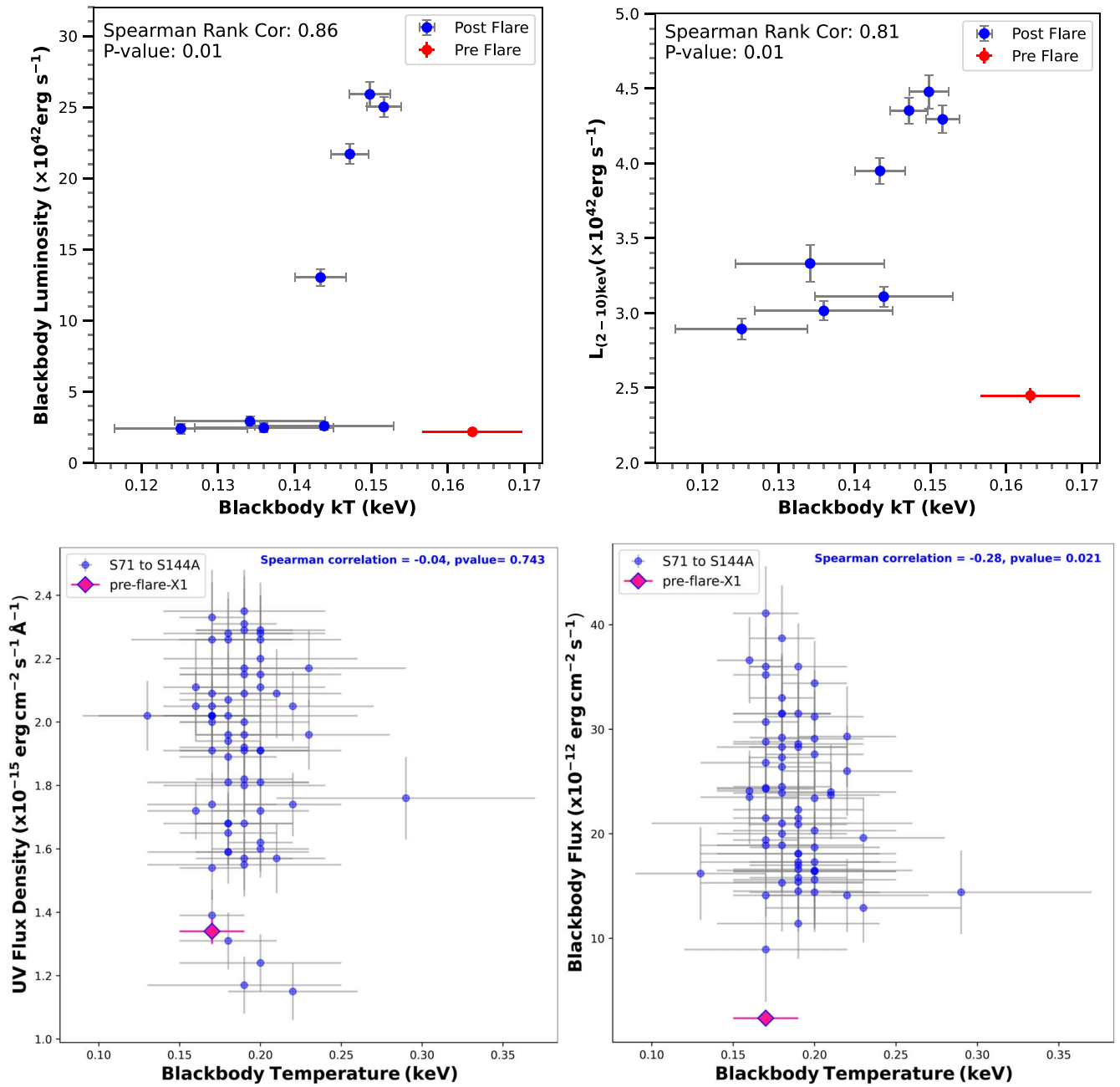


Figure A2. The correlations between the best-fit blackbody temperature (kT_e) and the UV flux density, blackbody luminosity (XMM-Newton), blackbody flux (Swift), and power-law luminosity (XMM-Newton). Top left: the blackbody temperature vs. the UVW2 monochromatic flux density. Top right: the blackbody temperature vs. power-law luminosity (XMM-Newton). Bottom left: the blackbody temperature vs. the UV flux density, Bottom right: the blackbody temperature vs. blackbody flux (Swift). We find that the blackbody temperature is very narrowly constrained, and we do not detect any significant correlation between these parameters.

ORCID iDs

Sibasish Laha <https://orcid.org/0000-0003-2714-0487>
 Eileen T. Meyer <https://orcid.org/0000-0002-7676-9962>
 Dev R. Sadaula <https://orcid.org/0000-0002-9163-8653>
 Ritesh Ghosh <https://orcid.org/0000-0003-4790-2653>
 Dhrubojyoti Sengupta <https://orcid.org/0009-0002-6991-1534>
 Megan Masterson <https://orcid.org/0000-0003-4127-0739>
 Onic I. Shuvo <https://orcid.org/0000-0003-4727-2209>
 Matteo Guainazzi <https://orcid.org/0000-0002-1094-3147>
 Claudio Ricci <https://orcid.org/0000-0001-5231-2645>

Mitchell C. Begelman <https://orcid.org/0000-0003-0936-8488>
 Alexander Philippov <https://orcid.org/0000-0001-7801-0362>
 Rostom Mbarek <https://orcid.org/0000-0001-9475-5292>
 Amelia M. Hankla <https://orcid.org/0000-0001-9725-5509>
 Erin Kara <https://orcid.org/0000-0003-0172-0854>
 Francesca Panessa <https://orcid.org/0000-0003-0543-3617>
 Ehud Behar <https://orcid.org/0000-0001-9735-4873>
 Haocheng Zhang <https://orcid.org/0000-0001-9826-1759>
 Fabio Pacucci <https://orcid.org/0000-0001-9879-7780>
 Main Pal <https://orcid.org/0000-0001-6523-6522>

Federica Ricci  <https://orcid.org/0000-0001-5742-5980>
 Ilaria Villani  <https://orcid.org/0009-0006-7483-0463>
 Susanna Bisogni  <https://orcid.org/0000-0003-3746-4565>
 Fabio La Franca  <https://orcid.org/0000-0002-1239-2721>
 Stefano Bianchi  <https://orcid.org/0000-0002-4622-4240>
 Gabriele Bruni  <https://orcid.org/0000-0002-5182-6289>
 Samantha Oates  <https://orcid.org/0000-0001-9309-7873>
 Matt Nicholl  <https://orcid.org/0000-0002-2555-3192>
 S. Bradley Cenko  <https://orcid.org/0000-0003-1673-970X>
 Sabyasachi Chattopadhyay  <https://orcid.org/0000-0003-1601-8048>
 Josefa Becerra González  <https://orcid.org/0000-0002-6729-9022>
 J. A. Acosta–Pulido  <https://orcid.org/0000-0002-0433-9656>
 Suvendu Rakshit  <https://orcid.org/0000-0002-8377-9667>
 Jiří Svoboda  <https://orcid.org/0000-0003-2931-0742>
 Luigi Gallo  <https://orcid.org/0009-0006-4968-7108>
 Adam Ingram  <https://orcid.org/0000-0002-5311-9078>
 Darshan Kakkad  <https://orcid.org/0000-0002-2603-2639>

References

- Abdollahi, S., Acero, F., Ackermann, M., et al. 2020, *ApJS*, 247, 33
 Baskin, A., & Laor, A. 2021, *MNRAS*, 508, 680
 Begelman, M. C., Scepi, N., & Dexter, J. 2022, *MNRAS*, 511, 2040
 Bellm, E. C., Kulkarni, S. R., Graham, M. J., et al. 2019, *PASP*, 131, 018002
 Belloni, T. M. 2010, *LNP*, 794, 53
 Beloborodov, A. M. 2017, *ApJ*, 850, 141
 Bianchi, S., Panessa, F., Barcons, X., et al. 2012, *MNRAS*, 426, 3225
 Blandford, R. D., & Payne, D. G. 1982, *MNRAS*, 199, 883
 Blandford, R. D., & Znajek, R. L. 1977, *MNRAS*, 179, 433
 Blumenthal, G. R., & Gould, R. J. 1970, *RvMP*, 42, 237
 Boller, T., Voges, W., Dennefeld, M., et al. 2003, *A&A*, 397, 557
 Burrows, D. N., Hill, J. E., Nousek, J. A., et al. 2005, *SSRv*, 120, 165
 Casella, P., Belloni, T., & Stella, L. 2005, *ApJ*, 629, 403
 Corbel, S., Kaaret, P., Jain, R. K., et al. 2001, *ApJ*, 554, 43
 Crummy, J., Fabian, A. C., Gallo, L., & Ross, R. R. 2006, *MNRAS*, 365, 1067
 Dai, X., Kochanek, C. S., Chartas, G., et al. 2010, *ApJ*, 709, 278
 Dexter, J., & Begelman, M. C. 2019, *MNRAS*, 483, L17
 Done, C., Davis, S. W., Jin, C., Blaes, O., & Ward, M. 2012, *MNRAS*, 420, 1848
 Done, C., Gierliński, M., & Kubota, A. 2007, *A&ARv*, 15, 1
 Duras, F., Bongiorno, A., Ricci, F., et al. 2020, *A&A*, 636, A73
 Eardley, D. M., Lightman, A. P., & Shapiro, S. L. 1975, *ApJL*, 199, L153
 Elvis, M., Wilkes, B. J., McDowell, J. C., et al. 1994, *ApJS*, 95, 1
 Evans, P. A., Beardmore, A. P., Page, K. L., et al. 2009, *MNRAS*, 397, 1177
 Fabian, A. C. 2012, *ARA&A*, 50, 455
 Fabian, A. C., Zoghbi, A., Ross, R. R., et al. 2009, *Natur*, 459, 540
 Gallo, E., Corbel, S., Fender, R. P., Maccarone, T. J., & Tzioumis, A. K. 2004, *MNRAS*, 347, L52
 Gallo, L. C., MacMackin, C., Vasudevan, R., et al. 2013, *MNRAS*, 433, 421
 García, J., Dauser, T., Lohfink, A., et al. 2014, *ApJ*, 782, 76
 García, J. A., Steiner, J. F., McClintock, J. E., et al. 2015, *ApJ*, 813, 84
 Gdel, M., & Benz, A. O. 1993, *ApJL*, 405, L63
 Ghosh, R., Laha, S., Meyer, E., et al. 2023, *ApJ*, 955, 3
 Gierliński, M., Middleton, M., Ward, M., & Done, C. 2008, *Natur*, 455, 369
 Graham, M. J., Kulkarni, S. R., Bellm, E. C., et al. 2019, *PASP*, 131, 078001
 Grošelj, D., Hakobyan, H., Beloborodov, A. M., Sironi, L., & Philippov, A. 2024, *PhRvL*, 132, 085202
 Homan, J., Bright, J., Motta, S. E., et al. 2020, *ApJL*, 891, L29
 Hovatta, T., Tornikoski, M., Lainela, M., et al. 2007, *A&A*, 469, 899
 Ingram, A. R., & Motta, S. E. 2019, *NewAR*, 85, 101524
 Jansen, F., Lumb, D., Altieri, B., et al. 2001, *A&A*, 365, L1
 Kalberla, P. M. W., Burton, W. B., Hartmann, D., et al. 2005, *A&A*, 440, 775
 Kara, E., Cackett, E. M., Fabian, A. C., Reynolds, C., & Uttley, P. 2013, *MNRAS*, 439, L26
 Katz, J. I. 1976, *ApJ*, 206, 910
 Kormendy, J., & Ho, L. C. 2013, *ARA&A*, 51, 511
 Laha, S., Markowitz, A. G., Krumpe, M., et al. 2020, *ApJ*, 897, 66
 Laha, S., Meyer, E., Roychowdhury, A., et al. 2022, *ApJ*, 931, 5
 Laha, S., Ricci, C., Mather, J. C., et al. 2024, *arXiv:2412.11321*
 LaMassa, S. M., Cales, S., Moran, E. C., et al. 2015, *ApJ*, 800, 144
 Laor, A., & Behar, E. 2008, *MNRAS*, 390, 847
 Li, R., Ho, L. C., Ricci, C., et al. 2022, *ApJ*, 933, 70
 Li, R., Ricci, C., Ho, L. C., et al. 2024, *ApJ*, 975, 140
 Lisakov, M., Jorstad, S., Wielgus, M., et al. 2025, *A&A*, 693, A9
 Liska, M. T. P., Musoke, G., Tchekhovskoy, A., Porth, O., & Beloborodov, A. M. 2022, *ApJL*, 935, L1
 Madau, P., & Haardt, F. 2024, *ApJL*, 976, L24
 Marti-Vidal, I., Muller, S., Vlemmings, W., Horellou, C., & Aalto, S. 2015, *Sci*, 348, 311
 Masterson, M., Kara, E., Ricci, C., et al. 2022, *ApJ*, 934, 35
 Masterson, M., Kara, E., Panagiotou, C., et al. 2025, *Natur*, 638, 370
 Mayer, M., & Pringle, J. E. 2007, *MNRAS*, 376, 435
 Merloni, A., & Fabian, A. C. 2001, *MNRAS*, 321, 549
 Meyer, E. T., Laha, S., Shuvo, O. I., et al. 2025, *ApJL*, 979, L2
 Miller-Jones, J. C. A., Sivakoff, G. R., Altamirano, D., et al. 2012, *MNRAS*, 421, 468
 Novikov, I. D., & Thorne, K. S. 1973, *Black Holes (Les Astres Occlus)* (New York: Gordon & Breach), 343
 O’Sullivan, S. P., & Gabuzda, D. C. 2009, *MNRAS*, 400, 26
 Pacucci, F., & Narayan, R. 2024, *ApJ*, 976, 96
 Panessa, F., Barcons, X., Bassani, L., et al. 2007, *A&A*, 467, 519
 Panessa, F., & Bassani, L. 2002, *A&A*, 394, 435
 Pasham, D. R., Remillard, R. A., Fragile, P. C., et al. 2019, *Sci*, 363, 531
 Pozdnyakov, L. A., Sobol, I. M., & Syunyaev, R. A. 1977, *SvA*, 21, 708
 Remillard, R. A., Muno, M. P., McClintock, J. E., & Orosz, J. A. 2002, *ApJ*, 580, 1030
 Ricci, C., Kara, E., Loewenstein, M., et al. 2020, *ApJL*, 898, L1
 Ricci, C., Loewenstein, M., Kara, E., et al. 2021, *ApJS*, 255, 7
 Ricci, C., & Trakhtenbrot, B. 2023, *NatAs*, 7, 1282
 Ricci, C., Trakhtenbrot, B., Koss, M. J., et al. 2017, *ApJS*, 233, 17
 Roming, P. W. A., Kennedy, T. E., Mason, K. O., et al. 2005, *SSRv*, 120, 95
 Russell, T. D., Tetarenko, A. J., Miller-Jones, J. C. A., et al. 2019, *ApJ*, 883, 198
 Saccheo, I., Bongiorno, A., Piconcelli, E., et al. 2023, *A&A*, 671, A34
 Scepi, N., Begelman, M. C., & Dexter, J. 2021, *MNRAS*, 502, L50
 Shakura, N. I., & Sunyaev, R. A. 1973, *A&A*, 24, 337
 Strüder, L., Briel, U., Dennerl, K., et al. 2001, *A&A*, 365, L18
 Tchekhovskoy, A., Narayan, R., & McKinney, J. C. 2011, *MNRAS*, 418, L79
 Terashima, Y., & Wilson, A. S. 2003, *ApJ*, 583, 145
 Tortosa, A., Bianchi, S., Marinucci, A., Matt, G., & Petrucci, P. O. 2018, *A&A*, 614, A37
 Tortosa, A., Ricci, C., Ho, L. C., et al. 2023, *MNRAS*, 519, 6267
 Trakhtenbrot, B., Arcavi, I., MacLeod, C. L., et al. 2019, *ApJ*, 883, 94
 Vaia, B., Ursini, F., Matt, G., et al. 2024, *A&A*, 688, A189
 Vasudevan, R. V., & Fabian, A. C. 2007, *MNRAS*, 381, 1235
 Wilkins, D. R., Gallo, L. C., Costantini, E., Brandt, W. N., & Blandford, R. D. 2021, *Natur*, 595, 657
 Zappacosta, L., Piconcelli, E., Fiore, F., et al. 2023, *A&A*, 678, A201